

Internal tides off the Amazon shelf Part I: importance for the structuring of ocean temperature during two contrasted seasons

Fernand Assene ¹, Ariane Koch-Larrouy ², Isabelle Dadou ³, Michel Tchilibou ⁴, Guillaume Morvan ⁵, Jérôme Chanut ⁶, Alex Costa da Silva ⁷, Vincent Vantrepotte ⁸, Damien Allain ⁹, Trung-Kien Tran ¹⁰

^{1,2,3,5,9} Université de Toulouse, LEGOS (CNRS/IRD/UPS/CNES), Toulouse, France

^{1,6} Mercator Ocean International, 31400, Toulouse, France

⁴ Collecte Localisation Satellites (CLS), 31500, Ramonville Saint-Agne, France

⁷ Departamento de Oceanografia da Universidade Federal de Pernambuco, DOCEAN/UFPE, Recife, Brazil

^{8,10} Laboratoire d'Océanologie et de Géosciences (LOG), 62930, Wimézeux, France

Correspondence to: Fernand Assene fassene@mercator-ocean.fr

Abstract

The impact of the tides (internal and external) on the vertical and horizontal structure of temperature off the Amazon River is investigated during two highly contrasted seasons (AMJ : April-May-June and ASO: August-September-October) over a three-year period from 2013 to 2015. Twin regional simulations with and without tides are used to highlight the general effect of tides. The tides tend to cool down the ocean from the surface (~ 0.3 °C) to above the thermocline (~ 1.2 °C), and to warm it up below the thermocline (~ 1.2 °C). The heat budget analysis leads to the conclusion that vertical mixing represents the dominant process that drives these temperature variations within the mixed layer, while it is associated with both horizontal and vertical advection below to explain temperature variations. The intensified mixing in the simulation including tides is attributed to the breaking of internal tides (IT) on their generation sites over the shelf break and offshore along their propagation pathways. While over the shelf, the mixing is driven by the dissipation of the external tides. In addition, vertical terms of the heat budget equation show wavelength patterns typical of mode-1 IT.

Moreover, we found that the tides can impact the interactions between the upper ocean interface and the overlying atmosphere. They account for a significant proportion of the net heat flux between the atmosphere and the ocean, with a marked seasonal variation of 33.2% in AMJ to 7.4% in ASO seasons. Tidal dynamics is therefore critical to understand the climate at

32 regional scale. This study highlights the key role of tides and particularly how IT-related vertical
33 mixing helps to shape ocean temperature off the Amazon.

34 **Keywords:** Amazon shelf break, internal tides, mixing, temperature, heat flux, modeling,
35 satellite data.

36 **I. Introduction**

37 Temperature and its spatial structure play a crucial role in ocean, including water mass
38 formation (Swift and Aagaard, 1981; Lascaratos, 1993; Speer et al., 1995), transport and mixing
39 of other tracers in the ocean and exchanges with other biosphere compartments (Archer et al.,
40 2004, Rosenthal et al., 1997), and most importantly on surface heat exchange at the interface
41 with the atmosphere (Clayson and Bogdanoff, 2013; Mei et al., 2015) and can thus significantly
42 influence the climate (Li et al., 2006; Collins et al., 2010). This oceanic thermal structure can
43 be modified at various spatial and temporal scales, through different processes external to the
44 ocean like solar radiation, heat exchanges with the atmosphere, winds, precipitation, and
45 freshwater inputs from rivers, and by its internal processes such as mass transport by currents
46 and eddies (e.g., Aguedjou et al., 2021), mixing by turbulent diffusion (Kunze et al., 2012), the
47 dissipation of internal waves (Barton et al., 2001; Smith et al., 2004; Salamena et al., 2021).
48 Finally, bottom friction of the barotropic tidal currents may also produce intensified mixing
49 especially for shallow water conditions (e.g., over a shelf, see Lambeck and Runcorn, 1977; Le
50 Provost and Lyard, 1997) and significantly modify ocean temperature in surface layers (Li et
51 al., 2020).

52 The barotropic tides, also called external tides, are the main source for internal waves
53 generation. The external tides, when interacting with sharp topography (e.g., ridge, sea mounts,
54 shelf break) in a stratified ocean, generate internal tides, that propagate and dissipate in the
55 ocean interior causing diapycnal mixing (Baines, 1982; Munk and Wunsch, 1998; Egbert and
56 Ray, 2000). A number of observational and modelling studies have shown that this dissipation
57 occurs at the generation sites, at the reflection to the bottom or close to the surface when the
58 energy rays interact with the thermocline and pycnocline (among others: Laurent and Garrett,
59 2002; Sharples et al., 2007, 2009; Koch-Larrouy et al., 2015; Nugroho et al., 2018; Whalen et
60 al., 2012). IT also dissipate or lose energy by wave-wave interactions or when they interact with
61 mesoscale or fine-scale structures (Vlasenko and Stashchuk, 2006; Dunphy and Lamb, 2014).

62 The role of internal tides on the ocean's thermal structure has been the subject of
63 growing interest and numerous studies in recent years. In the Hawaii shallow shelf surface

64 waters, Smith et al. (2016) report that IT can induce surface cooling from 1 °C to 5 °C. For the
65 Indonesian region, IT induce an annual mean surface cooling of 0.5 °C (Koch-Larrouy et al.,
66 2007, 2008; Nagai and Hibiya, 2015 and Nugroho et al., 2018) that decreases local atmospheric
67 convection, which in turn reduces precipitation by 20%. They can therefore fulfil a relevant role
68 on regional climate (Koch-Larrouy et al., 2010; Sprintall et al., 2014, 2019). Furthermore, in
69 the Andaman Sea, Jithin and Francis (2020) showed that internal tides can affect the
70 temperature in deep waters (> 1600 m), leading to a warming of about 1–2 °C. But off the
71 Amazon plateau, their impact on the thermal structure of the ocean is still poorly understood.

72 Our study focuses on the oceanic region of northern Brazil off the Amazon River. This
73 region exhibits a variation in the wind position and hence the position of the Intertropical
74 Convergence Zone (ITCZ) during the year. This directly influences the discharge of the
75 Amazon River, oceanic circulation, eddy kinetic energy (EKE) and the stratification (Muller-
76 Karger et al., 1988; Johns et al., 1990; Xie and Carton, 2004). Hence, two very contrasting
77 seasons form, April-May-June (AMJ) and August-September-October (ASO). AMJ (vs. ASO)
78 is characterized by an increasing (vs. decreasing) river discharge, stronger (vs. smaller) and
79 shallower (vs. deeper) pycnocline. The North Brazilian Current (NBC) and eddy kinetic energy
80 (EKE) are weaker (vs. stronger) (Aguedjou et al., 2019, Tchilibou et al., 2022). For the ASO
81 season, the stronger NBC develops a retroflection (NBCR) between 5°–8° N that feeds the
82 North Equatorial Counter-Current (NECC) transporting the water masses towards the east of
83 the tropical Atlantic. The retroflection also generates very large anticyclonic eddies (NBC
84 Rings) exceeding 450 km in diameter (Didden and Schott, 1993; Richardson et al., 1994;
85 Garzoli et al., 2003), which in turn transport water masses towards the Northern Hemisphere
86 (Bourles et al., 1999; Johns et al., 1998; Schott et al., 2003).

87 Internal tides are generated on the sharp shelf break featured by a depth decreasing from
88 200-2000 m over some tens of kilometers (Fig.1). Six main sites (A to F) have been identified,
89 with the most intense, A and B, located in the southern part of the region (Fig.1; Magalhaes et
90 al., 2016, Tchilibou et al., 2022). Previous studies have shown that in this region IT propagation
91 is modulated by the seasonal variation of the currents (Magalhaes et al., 2016; Lentini et al.,
92 2016; Tchilibou et al., 2022). In addition, seasonal variations in stratification induce changes in
93 the internal tide's activity, with in AMJ (vs. ASO) a stronger (vs. smaller) energy conversion
94 and a stronger (vs. smaller) local dissipation of IT energy (Barbot et al., 2021, Tchilibou et al.,
95 2022). The interaction between the weaker (vs. stronger) background circulation and IT leads
96 to less (vs. more) incoherent or non-stationary internal tides (Tchilibou et al., 2022).

97 During the ASO season, cold water (< 27.6 °C) associated with the western extension
98 of the Atlantic Cold-water Tongue (ACT) runs the region from the south and run along the edge
99 of the continental shelf to about 3°N , establishing a cold cell often referred to as seasonal
100 upwelling (Lentz and Limeburner, 1995; Neto and da Silva, 2014). Modelling studies, with and
101 without tides, have shown that this upwelling is affected by the tides. Cooling is more realistic
102 when tides are included (Ruault et al., 2020). However, these analyses cannot determine what
103 processes are at work. For example, it is not yet explicit whether the tidal-induced cooling is
104 due to mixing on the shelf produced by barotropic tides, or to the mixing produced by baroclinic
105 tides at their generation sites and propagation pathways. Based on *in situ* observations, Neto
106 and da Silva (2014) suggest instead that it is the vertical advection triggered by the NBC that
107 can explain the cooling observed at the surface.

108 To answer the previous questions, we use a high-resolution model ($1/36^{\circ}$) with and
109 without explicit tidal forcing and a satellite SST product, with the aim of highlighting the impact
110 of tides on the temperature structure and quantify the associated processes. We distinguish the
111 analysis for the two contrasted seasons (AMJ and ASO) described above. The SST product, our
112 model, and the methods used are described in section II. The validation of certain characteristics
113 of the barotropic and baroclinic tides and of the temperature is presented in section III. The
114 impacts of IT on the temperature structure, the influence on heat exchange at the atmosphere-
115 ocean interface, and the processes involved, are analyzed in section IV. The discussion and the
116 summary of the obtained results are presented in section V and VI respectively.

117 **II. Data and Methods**

118 **II.1. Satellite Data: TMI SST**

119 This dataset is derived from Tropical Rainfall Measurement Mission (TRMM), which
120 performs measurements using onboard TRMM Microwave Imager (TMI). The microwaves can
121 penetrate clouds and are therefore crucially important for data acquisition in low latitude
122 regions, cloudy covered during long periods of raining seasons. We use TMI data products v7.1,
123 which represents the most recent version of TMI SST. It contains a daily mean of SST with a
124 $0.25^{\circ}\times 0.25^{\circ}$ grid resolution (~ 25 km). This SST is obtained by inter-calibration of TMI data
125 with other microwave radiometers. The TMI SST full description and inter-calibration
126 algorithm are detailed in Wentz (2015).

127 **II.2. The NEMO Model: *AMAZON36* configuration**

128 The numerical model used in this study is the Nucleus for European Modelling of the
129 Ocean (NEMOv4.0.2, Madec et al., 2019). The configuration designed for our purpose is called
130 *AMAZON36* and covers the western tropical Atlantic region from the Amazon River mouth to
131 the open ocean. Other configurations exist in this region, but either they have a coarse grid ($1/4^\circ$
132 , Hernandez et al., 2016), or when the grid is fine ($1/36^\circ$) they do not extend very far eastwards
133 and therefore exclude most of the site B (Ruault et al., 2020). The current configuration avoids
134 these two limitations. The grid resolution is $1/36^\circ$ and the domain lies between 54.7°W – 35.3°W
135 and 5.5°S – 10°N (Fig.1). In this way, we capture the internal tides radiating from all the
136 generating sites on the Brazilian shelf break. The vertical grid comprises 75 vertically fixed z-
137 coordinates levels, with a narrower grid refinement near the surface with 23 levels in the first
138 100 m. Cell thickness reaches 160 m when approaching the bottom. The horizontal and vertical
139 resolutions of the grid are therefore fine enough to resolve low-mode internal tides. This grid
140 resolution has already been used for this purpose in this region (e.g., Tchilibou et al., 2022).

141 A third order upstream biased scheme (UP3) with built-in diffusion is used for
142 momentum advection, while tracer advection relies on a 2nd order Flux Corrected Transport
143 (FCT) scheme (Zalesak, 1979). A Laplacian isopycnal diffusion with a constant coefficient of
144 $20\text{ m}^2\cdot\text{s}^{-1}$ is used for tracers. The temporal integration is achieved thanks to a leapfrog scheme
145 combined with an Asselin filter to damp numerical modes, with a baroclinic time step of 150 s.
146 The \mathcal{K} – \mathcal{E} turbulent closure scheme is used for vertical diffusion. Bottom friction is quadratic
147 with a bottom drag coefficient of 2.5×10^{-3} , while lateral wall free-slip boundary conditions are
148 prescribed. A time splitting technique is used to resolve the free surface, with the barotropic
149 part of the dynamical equations integrated explicitly.

150 We use the 2020's release of the General Bathymetric Chart of the Oceans interpolated
151 onto the model horizontal grid, with the minimal depth set to 12.8 m. The model is forced at
152 the surface by the ERA-5 atmospheric reanalysis (Hersbach et al., 2020). The river discharges
153 are based on monthly means from hydrology simulation of the Interaction Sol-Biosphère-
154 Atmosphère model (see details in <https://www.umr-cnrm.fr/spip.php?article146&lang=en>) and
155 are prescribed as surface mass sources with null salinity, and we use a multiplicative factor of
156 90% based on a comparison with the HYBAM interannual timeseries (see details in
157 <http://www.ore-hybam.org>). The model is forced at its open boundaries by the fifteen major
158 tidal constituents (M_2 , S_2 , N_2 , K_2 , $2N_2$, MU_2 , NU_2 , L_2 , T_2 , K_1 , O_1 , Q_1 , P_1 , S_1 , and M_4) and
159 barotropic currents, derived from FES2014 atlas (Lyard et al., 2021). In addition to the open

160 boundaries, we prescribe the recent MERCATOR-GLORYS12 v1 assimilation data (Lellouche
161 et al., 2018) for temperature, salinity, sea level, current velocity and derived baroclinic velocity.

162 The simulation was initialized on the 1st of January 2005, and ran for 11 years until
163 December 2015. In this study, we use three-year model outputs from January 2013 to December
164 2015. Indeed, the model has reached an equilibrium in terms of seasonal cycle after 2 years. A
165 twin model configuration without tides is used to highlight the influence of tides on the
166 temperature structure.

167 **II.3. Methods**

168 **II.3.1. Tide energy budget**

169 We follow Kelly et al. (2010) to separate barotropic and baroclinic tide constituents.
170 There is no separation following vertical modes, then we analyze the total energy for all the
171 resolved propagation modes for a given tidal frequency. Note that the barotropic/baroclinic tide
172 separation is performed directly by the model for better accuracy. We have only analyzed the
173 M_2 harmonic which is the major tidal constituent in this region (Prestes et al., 2018; Fassoni-
174 Andrade et al., 2023), representing $\sim 70\%$ of the tidal energy (Beardsley et al., 1995; Gabioux
175 et al., 2005).

176 The barotropic and baroclinic tide energy budget equations are obtained assuming that
177 the energy tendency, the nonlinear advection and the forcing terms are small (Wang et al.,
178 2016). Then, the remaining equations are reduced to the balance between the energy dissipation,
179 the divergence of the energy flux, and the energy conversion from barotropic to baroclinic (e.g.,
180 Buijsman et al., 2017; Tchilibou et al., 2018, 2020; Jithin and Francis, 2020; Peng et al., 2021)
181 :

$$182 \quad D_{bt} + \nabla_h \cdot F_{bt} + C \approx 0 \quad (1)$$

$$183 \quad D_{bc} + \nabla_h \cdot F_{bc} - C \approx 0 \quad (2)$$

184 bt and bc indicate the barotropic and baroclinic terms, D is the depth-integrated energy
185 dissipation, which can be understood as a proxy of the real dissipation since D may encompass
186 the energy loss of non-linear terms and/or numerical dissipation (see Nugroho et al., 2018), ∇_h
187 $\cdot F$ represents the divergence of the depth-integrated energy flux, whilst C is the depth-integrated
188 barotropic-to-baroclinic energy conversion, i.e., the amount of incoming barotropic energy
189 converted into internal tides energy over the steep topography, with:

190 $C = \langle \nabla H \cdot U_{bt} P_{bc}^* \rangle$ (3)

191 $F_{bt} = \langle U_{bt} P_{bt} \rangle$ (4)

192 $F_{bc} = \int_H^\eta \langle U_{bc} P_{bc} \rangle dz$ (5)

193 where the angle bracket $\langle \cdot \rangle$ denotes the average over a tidal period, ∇H is the slope of the
 194 bathymetry, U is the current velocity, P_{bc}^* is the baroclinic pressure perturbation at the bottom,
 195 H is the bottom depth, η the surface elevation, P is the pressure, then F is the energy flux and
 196 emphasizes the path of the tides.

197 II.3.2. 3-D heat budget equation for temperature

198 The three-dimensional temperature budget was computed online and further analyzed.
 199 It is the balance between the total temperature trend and the sum of the temperature advection,
 200 diffusion and solar radiative and non-solar radiative fluxes (e.g., Jouanno et al., 2011;
 201 Hernandez et al., 2017):

202
$$\partial_t T = \underbrace{-u\partial_x T - v\partial_y T - w\partial_z T}_{ADV} + LDF - \underbrace{\partial_z(K_z\partial_z T)}_{ZDF} + Forcing + Asselin$$
 (6)

203 Here T is the model potential temperature, (u, v, w) are the velocity components in the (x, y, z)
 204 [respectively eastward, northward and upward] directions, ADV is the 3-D tendency term from
 205 the advection routine of the NEMO code (from the left to right: zonal, meridional and vertical
 206 terms). Note that in our model, ADV includes nonlinear effect between the temperature and the
 207 currents and leads to some diffusivity of the temperature due to numerical dissipation of the
 208 FCT advection scheme (Zalesak, 1979) in contrast to some non-diffusive advection scheme like
 209 in Leclair and Madec (2009). In previous studies, for lower resolution ($1/4^\circ$), this mixing has
 210 been quantified to be responsible for 30% of the dissipation as part of the high-frequency work
 211 of the diffusion (Koch-Larrouy et al., 2008). We expect here at $1/36^\circ$ resolution that this effect
 212 will be smaller but still non negligible. This will be discussed in the last section. Note that
 213 explicit separation of this effect is beyond the scope of our study. Furthermore, ZDF represents
 214 the vertical diffusion, LDF is the lateral diffusion, $Forcing$ is the sum of tendency of
 215 temperature due to penetrative solar radiation, which includes a vertical decaying structure, and
 216 the non-solar heat flux (sum of the latent, sensible, and net infrared fluxes) at the surface layer,
 217 and $Asselin$ corresponds to the numerical diffusion for the temperature.

218 **III. Model validation**

219 In this subsection, we assess the quality of our simulations by verifying whether they
220 are in good agreement with the observations and other reference data. Firstly, for the barotropic
221 and baroclinic characteristics of the M_2 tides for the year 2015, and finally for the temperature
222 from 2013 to 2015.

223 **III.1. M_2 Tides in the model**

224 We initially examined the barotropic SSH and there is a good agreement in both
225 amplitude (color shading) and phase (solid contours) between FES2014 and the model, Fig.2a
226 and Fig.2b respectively. Nevertheless, near the coast, some differences are observed in
227 amplitude. The SSH amplitude of the model is lower ($\sim +50$ cm) north of the mouth of the
228 Amazon. However, shoreward and on the southern part of the mouth, the model overestimates
229 the amplitude by $\sim +20$ cm and $\sim +40$ cm respectively. These biases are of the same order of
230 magnitude as Ruault et al. (2020). The flux of the barotropic tidal energy flowing inshore is
231 represented by the black arrows in Fig.2c and Fig.2d for FES2014 and the model respectively.
232 A fraction of this energy is converted into baroclinic tidal energy over the steep slope of the
233 bathymetry. We compared the depth-integrated barotropic-to-baroclinic energy conversion rate
234 (C) between FES2014 and the model, color shading in Fig.2c and Fig.2d respectively. The
235 model does reproduce the same conversion patterns of FES2014 over the slope, but hardly
236 offshore between 42°W – 35°W and 7°N – 10°N . This leads to an overall underestimate of C of
237 about 30% by our model. Niwa and Hibiya (2011) have shown that C increases with bathymetry
238 resolution, meaning that there is more conversion with the FES2014 grid (~ 1.5 km) compared
239 to our grid (~ 3 km). In addition, FES2014 (vs. our model) is a barotropic (vs. baroclinic) model,
240 which may be a source of some differences since it solves different set of equations.

241 Another part of the barotropic energy is dissipated on the shelf by bottom friction and
242 induces mixing from the bottom (Beardsley et al., 1995; Gabioux et al., 2005; Bessières, 2007;
243 Fontes et al. (2008). Most of the dissipation of barotropic energy (D_{bt}) occurs in the middle and
244 inner shelf between 3°S – 4°N (Fig.2e) in good agreement with Beardsley et al. (1995) and
245 Bessières (2007). The remaining barotropic energy propagates over hundreds of kilometers into
246 the estuarine systems of this region (Kosuth et al., 2009; Fassoni-Andrade et al., 2023).

247 For the internal tides, their energy flux (F_{bc} , black arrows in Fig.2f) shows that they
248 from the slope towards the open ocean. F_{bc} highlights the existence of six main sites of IT

249 generation on the slope. Two of these are more important (A and B) regarding their higher and
250 far extended energy flux, in good agreement with Magalhaes et al. (2016), Barbot et al. (2021)
251 and Tchilibou et al. (2022). From these two main sites, internal tides spread over nearly 1000
252 km, and dissipate their energy. Color shading in Figure 2f shows the model's depth-integrated
253 internal tides energy dissipation (D_{bc}). We found that about 30% of the energy is dissipated
254 locally over generation sites (not shown), in good agreement with Tchilibou et al. (2022). The
255 remaining part is dissipated offshore along the propagation path. This offshore dissipation is
256 more extended along path A, ~300 km from the slope, with two patterns spaced approximately
257 by an average wavelength of 120–150 km corresponding to mode-1 propagation. While there
258 is less offshore dissipation along path B, occurring around 100–200 km from the slope (Fig.2f).

259 Another critical characteristic of IT is their SSH imprints along the propagation
260 pathway. We compared an estimate of this signature deduced from the altimeter tracks (Fig.2g)
261 produced by Zaron (2019) with our model (Fig.2h), with shelf masked over 150 m depth. Our
262 model is in good agreement with this product, with an overestimation of the order of ~ +1.5 cm
263 on the SSH maxima. It is relevant to note that the baroclinic SSH of our model is an average
264 over the year 2015, whilst the estimate is an average over about 20 years. This means that the
265 variability of the altimeter tracks is greater due to the longer period, which may reduce the
266 amplitude of the estimates and explain the small differences in the positioning and amplitude
267 of the maxima.

268 **III.2. Temperature validation**

269 Figure 3 shows the mean SST over the entire 2013–2015 period for TMI SST (Fig.3a),
270 the tidal simulation (Fig.3b) and the non-tidal simulation (Fig.3c), then, the bias between TMI
271 SST and the two simulations is obtained by linear interpolation of the simulations data on the
272 observation grid. The simulation with tides accurately reproduces the spatial distribution of the
273 observations both for cooling on the shelf around 47.5°W and to the southeast between 40°W
274 –35°W and 2°S–2°N, as shown by the weak bias, $< \pm 0.1^\circ\text{C}$, with TMI (Fig.3d). This cooling is
275 inaccurately reproduced by the non-tidal simulation which exhibits a warm bias of about 0.3°C
276 (Fig.3.e). To the northeast, between 50°W–54°W and 3°N–8°N in the Amazon plume, the SST
277 of the non-tidal simulation is in better agreement with the observations, while the SST of the
278 tidal simulation is about $> 0.6^\circ\text{C}$ cooler than TMI SST (Fig.3d). The same bias is obtained in
279 this northern zone by other models including tides (e.g., Hernandez et al., 2016, 2017;
280 Gévaudan et al. (2022)). Far offshore, between 50°W–40°W and 6°N–10°N, both simulations
281 reveal a negative bias of about $0.2\text{--}0.3^\circ\text{C}$ (Fig.3d-e). We averaged the observations and the

282 interpolated simulation data in the dashed box (see Fig.3a-c), with depth < 200 m masked. This
283 location is around IT generation sites and on part of their pathways. Then, we compute the
284 seasonal cycle of the three products (Fig.3f). The tidal and non-tidal simulations of the model
285 reproduce accurately both the seasonal cycle and the standard deviation of the observations,
286 with a low RMSE of $\sim 2 \cdot 10^{-2} \text{ }^\circ\text{C}$ and $\sim 4 \cdot 10^{-2} \text{ }^\circ\text{C}$, between TMI SST and tidal and non-tidal
287 simulation respectively, indicating the robustness of our model's simulations. Over the seasonal
288 cycle, it appears that the tidal simulation is closer to the observations from January to March,
289 July to September and November to December, while during the rest of the year, either the two
290 simulations are equally close, or the non-tidal simulation is closer.

291 To gain an insight into our model along the depth, we used the mean WOA2018
292 climatology (2005–2017) and simulation data (salinity and temperature) for the three years
293 2013–2015, averaged in the same region as in Fig.3f. Figure 3g shows the Temperature-Salinity
294 (T-S) diagram for WOA2018 and the two simulations. The data are averaged in the box as
295 before, and we use $\sigma_\theta [\rho - 1000]$ to represent the density contours, with ρ the water density.
296 Both simulations exhibit similar patterns with WOA2018 for deeper waters, i.e., $T < 17 \text{ }^\circ\text{C}$ and
297 $\sigma_\theta > 25.6 \text{ kg}\cdot\text{m}^{-3}$. However, there exist minor discrepancies for the surface layer waters, i.e., T
298 $> 17 \text{ }^\circ\text{C}$ and $22.4 > \sigma_\theta < 25.6 \text{ kg}\cdot\text{m}^{-3}$. At that level, the tidal simulation better reproduces the T-
299 S profile of the observations. These small differences between WOA2018 observations and the
300 two simulations, especially with the tidal simulation, further demonstrate the ability of our
301 model to reproduce the observed water mass properties.

302 **IV. Results**

303 In this section, we present the influence of tides on the temperature, the associated
304 processes, and the impact on the atmosphere-ocean net heat exchange. The analyses were
305 performed on a seasonal scale between April-May-June (AMJ) and August-September-October
306 (ASO) for the three years 2013–2015.

307 **IV.1. Tide-enhanced surface cooling**

308 During the first season, warm waters, which are defined as $> 27.6^\circ\text{C}$, dominate near the
309 coast, especially in the middle shelf and in the south-east, and cold waters are present offshore
310 north of 6°N (Fig.4a-c). Off the mouth of the Amazon River, water colder than $28.2 \text{ }^\circ\text{C}$ spreads
311 between 43°W – 51°W for TMI SST (Fig.4a) and the tidal simulation (Fig.4b), while warmer
312 waters are present in the same area for the simulation without the tides (Fig.4c). Figures 4d-f
313 show the SST, averaged over the ASO season. The TMI SST observations (Fig.4d) shows an

314 upwelling cell represented by the extension of the 27.2 °C isotherm (white dashed contour)
315 along the slope to about 49°W–3°N towards the north-east of the region, which forms the
316 extension of the ACT. This extension also exists in the tidal simulation (Fig.4e), whereas ≤ 27.2
317 °C waters are not crossing 45.5°W and remain in the southern hemisphere in the simulation
318 without the tides (Fig.4f). This means that waters colder than 27.2°C can only extend further
319 into the northeast because of tides. In addition, we can note that the mean SST shows a very
320 contrasting distribution between the two seasons. There are warm waters along the shelf and
321 cold waters offshore during the AMJ season (Fig.4a-c). This is followed by warming along the
322 Amazon plume and offshore, and an upwelling cell in the south-east (Fig.4d-f).

323 The general impact of the tides, illustrated by the SST anomaly between the tidal and
324 the non-tidal simulation, is a cooling over a large part of the study area with maxima up to 0.3
325 °C (Fig. 5a-b). For ASO, tides induce a warming (> 0.3 °C) on the shelf at the mouth of the
326 Amazon River (Fig.5b), while for AMJ it is a cooling of the same intensity (Fig.5a). That
327 difference will be further discussed. Out of the shelf, the temperature anomaly for each season
328 has different spatial structures. This is probably due to a different mesoscale variability between
329 the two seasons.

330 **IV.2. Impact of the tides in the atmosphere-to-ocean net heat flux**

331 The atmosphere–ocean net heat flux (Q_t) reflects the balance of incoming and outgoing
332 heat fluxes across the atmosphere-ocean interface (see details on Moisan and Niiler, 1998;
333 Jayakrishnan and Babu, 2013). During AMJ, the tides mainly induce positive Q_t anomalies over
334 the whole domain. The average values are around 25 $W.m^{-2}$ in the plume and the Amazon
335 retroflection to the northeast and along A and B (Fig.5c). Negative SST anomalies ($\sim 0.3^\circ C$)
336 occur throughout the domain in the same location. During the ASO season, at the mouth of the
337 Amazon, there are negative Q_t anomalies but of the same magnitude as during the previous
338 season (Fig.5d). At this location, positive temperature anomalies ($\sim 0.3^\circ C$) are observed
339 (Fig.5b). Elsewhere, there are positive Q_t anomalies and negative SST anomalies. It therefore
340 appears that negative SST anomalies induce positive Q_t anomalies and vice versa. Hence, the
341 spatial structures of Q_t anomalies and SST anomalies fit almost perfectly together for the two
342 seasons. There is a strong negative correlation of 0.97 with a significance of $R^2 = 0.95$ for the
343 AMJ season. And roughly the same intensity and sign for the ASO season with 0.98 and 0.96,
344 respectively for the correlation and its significance (Fig.5e). This is consistent with the fact that
345 the atmosphere and the underlying ocean are balanced. Then, the SST cooling induced by

346 upwelled cold water will try upset this balance. As a result of this, an equivalent variation in
347 the net heat flux from the atmosphere to the ocean will attempt to restore it.

348 The integral over the entire domain of the net heat flux for each season and for each
349 simulation is shown in Figure 5f. During the AMJ season, Q_t increases from 23.85 TW (1 TW
350 = 10^{12} W) for the non-tidal simulation to 35.7 TW for the tidal simulation, i.e., an increase of
351 33.2 %. That is, the tides are responsible for a third of Q_t variation. This is very large compared
352 to what is observed elsewhere in other IT hotspots (e.g., 15% in Solomon Sea, Tchilibou et al.,
353 2020). During the second season, there is a smaller increase in Q_t of about 7.4% between the
354 two simulations, i.e., from 73.03 TW to 78.83 TW for the non-tidal and tidal simulations
355 respectively (Fig.5f).

356 It is also worth noting the significant difference in integrated Q_t between the two
357 seasons. The values are less than 36 TW during the AMJ season, whereas they are around twice
358 as high, > 73 TW, during the ASO season. Given that colder SST induce a stronger Q_t , these
359 higher values are likely related to the arrival of water from ACT, which forms upwelling cells
360 (Fig.4d-f) with a secondary tidal effect.

361 **IV.3. Vertical structure of Temperature along internal tides pathway**

362 To further analyze the temperature changes between both simulations, we made vertical
363 sections following the path of IT radiating from sites A and B (respectively black and red line
364 in Fig.2f). Hereunder, only the transects following the pathway A will be shown, since the
365 vertical structure is similar following pathway B especially for AMJ season and because some
366 processes tend to be null along pathway B during the ASO season. The mixed layer refers to a
367 quasi-homogenous surface layer of temperature-dependent density that interacts with the
368 atmosphere (Kara et al., 2003). Its maximum depth, also known as mixed-layer depth (MLD),
369 is defined as the depth where the density increases from the surface value, due to temperature
370 change of $|\Delta T| = 0.2$ °C with constant salinity (e.g., Dong et al., 2008; Varona et al., 2019).

371 Figure 6 shows the vertical sections of temperature for the two seasons following A. For
372 the AMJ season, over the slope and near the coast, cold waters (< 27.6 °C) remain below the
373 surface at ~ 20 m for the tidal simulation (Fig.6a) and deeper at ~ 60 m for the non-tidal
374 simulation (not shown). Then, cold waters rise to the surface more than 400 km offshore for
375 both simulations. At the surface the SST anomaly is relatively small (~ -0.3 °C, Fig.5a), because
376 the SST anomalies are likely damped by the heat fluxes, further down the water column, this
377 anomaly becomes much larger (Fig.6b). Above that thermocline (< 120 m), the simulation with
378 the tides is colder by 1.2 °C from the slope where IT are generated to the open ocean following

379 their propagation path. Conversely, below the thermocline, the tidal simulation is warmer by
380 approximately the same intensity ($1.2\text{ }^{\circ}\text{C}$) up to $\sim 300\text{ m}$ depth and along the propagation path
381 (Fig.6b). During this AMJ season, the thermocline is $\sim 100\text{ m} \pm 15\text{ m}$ deep and the MLD is ~ 40
382 $\text{m} \pm 20\text{ m}$ deep (dashed white line, Fig.6a). They both have a very weak slope between the coast
383 and the open ocean. Over the whole domain, the thermocline is deeper by about 15 m on average
384 in the non-tidal simulation, following the propagation paths of internal tides, on the Amazon
385 shelf and plume (Fig.6c). Whilst MLD in the non-tidal simulation is deeper by an average of
386 10 m over the shelf, 4 m on average along IT propagation paths and close to zero in the Amazon
387 plume (Fig.6d).

388 During the ASO season, cold waters previously confined below the surface during the
389 previous season (AMJ) rise to the surface. These cold waters extend over the slope and up to
390 about 150 km offshore in the non-tidal simulation (not shown) and up to 250 km offshore in the
391 tidal simulation (Fig.7a). The $27.2\text{ }^{\circ}\text{C}$ isotherm only reaches the surface above the slope in the
392 tidal simulation and remains below the surface ($\sim 30\text{ m}$) in the non-tidal simulation (not shown).
393 This aligns with the missing of that isotherm at this location in the corresponding SST map
394 (Fig.4f). For the tidal simulation, the temperature anomaly in the ASO season is smaller (< 0.4
395 $^{\circ}\text{C}$, Fig.7b) in the surface layers ($< 40\text{ m}$) near the coast compared to the AMJ season (Fig.6b).
396 In contrast, during the ASO season, this cooling can drive more SST anomalies along A (-0.3
397 $^{\circ}\text{C}$, Fig.5b). A stronger cooling of $\sim -1.2\text{ }^{\circ}\text{C}$ occurs deeper between 60 and 140 m depth, and a
398 warming of about $1.2\text{ }^{\circ}\text{C}$ below, which extends less offshore than during AMJ season, 650 km
399 vs. $\sim 1000\text{ km}$. During this ASO season, the coastward slope of the thermocline and MLD
400 becomes somewhat steeper compared to the other season. In both simulations, there is a dip of
401 $\sim 80\text{ m}$, i.e., $\sim 60\text{ m}$ offshore and $\sim 140\text{ m}$ inshore, for the thermocline (dashed black line, Fig.7a).
402 And a dip of $\sim 40\text{ m}$, i.e., $\sim 30\text{ m}$ offshore and $\sim 70\text{ m}$ inshore, for MLD (dashed white line,
403 Fig.7a). Over the entire domain, the tides reduce the thermocline depth by $\sim 6\text{ m}$ on the shelf
404 and $\sim 12\text{ m}$ at the plume and far offshore along the propagation path of A (Fig.7c). They reduce
405 the MLD in the tidal run by about 10 m along the shelf and $\sim 4\text{ m}$ along the propagation path of
406 A (Fig.7d).

407 Between the two seasons, there is also a change in the vertical density gradient between
408 the coast and the open sea. In the tidal simulation, during the AMJ season, the isopycnals layers
409 are tight near the coast and thicken towards the open sea (Fig.6a). This means that a strong
410 stratification is present near the coast and decreases towards the open sea. In contrast, during
411 the second ASO season, the isopycnals layers are thicker near the coast and tight offshore

412 (Fig.7a). As the result of this, the stratification is weaker inshore than offshore. This clearly
413 highlights a seasonality in the vertical density gradient profile in agreement with Tchilibou et
414 al. (2022). Note that this behavior also appears in the simulation without the tides (not shown).
415 The transects of the temperature anomaly, Fig.6b and 7b, show that the tides influence the
416 temperature in the ocean from the surface to the deep layers, with a greater effect on the first
417 300 meters. One question we address in this paper is to better understand what processes are at
418 work that explain these temperature changes.

419 **IV.4. What are the processes involved?**

420 To explain the observed surface and water column temperature changes, we computed
421 and analyzed the terms of the heat balance equation (see Section II.3.2, Equation 6) for both
422 seasons (AMJ and ASO).

423 **IV.4.1. Vertical diffusion of Temperature**

424 Figure 8 shows the vertical temperature diffusion tendency (ZDF). ZDF is averaged
425 between 2–20 m, i.e., within the mixed-layer. For the AMJ season, ZDF in the tidal simulation
426 (Fig.8a) shows a negative trend (cooling) in the whole domain. The maximum values ($> |0.4|$
427 $^{\circ}\text{C}\cdot\text{day}^{-1}$) are located along the slope where IT are generated and on their propagation path.
428 There is a larger horizontal extent along A of ~ 700 km from the coasts compared to B, where
429 it is ~ 300 km from the coasts. Elsewhere, it remains very low, > -0.1 $^{\circ}\text{C}\cdot\text{day}^{-1}$. For the non-tidal
430 simulation (Fig.8b), the ZDF is very weak over the entire domain (> -0.1 $^{\circ}\text{C}\cdot\text{day}^{-1}$). For the
431 ASO season, the tidal simulation (Fig.8c) shows a decrease of the ZDF near the coast (< 100
432 km) and a strengthening offshore along A compared to the previous season, but with the same
433 cooling trend (< -0.4 $^{\circ}\text{C}\cdot\text{day}^{-1}$). Along B, it tends to be null, both at the coast and offshore
434 (Fig.8c). In addition, the mesoscale circulation and eddy activity intensify during this season.
435 To the northeast, approximately between 4°N – 8°N , and 47°W – 53°W , there is a cooling on the
436 shelf of ~ 0.3 $^{\circ}\text{C}\cdot\text{day}^{-1}$ with eddy-like patterns in the tidal simulation (Fig.8c). The processes by
437 which these features might arise will be discussed in more details in section V. Unsurprisingly,
438 ZDF is very weak elsewhere for the non-tidal simulation (Fig.8d). Internal tides are the
439 dominant driver of vertical diffusion of temperature along the shelf break and offshore, while
440 the mixing induced by barotropic tides could prevail on the shelf.

441 On the vertical following A, there are opposite sign ZDF values, with mean magnitude
442 of $\sim |0.4|$ $^{\circ}\text{C}\cdot\text{day}^{-1}$. These values are centered around the thermocline for the simulation with
443 tides in the two seasons AMJ and ASO (respectively Fig.8e and 8f). There is a cooling trend

444 above the thermocline and a warming trend below. The average vertical extent is up to ~350 m
445 depth for the maximum values but exceeds 500 m depth for the low values ($< 0.1 \text{ }^\circ\text{C}\cdot\text{day}^{-1}$). As
446 for the horizontal averages (Fig.9a and 9c), from one season to another there is a weakening of
447 ZDF above the slope and a strengthening offshore, Fig.8e and 8f, for AMJ and ASO
448 respectively. Furthermore, offshore ZDF maxima seem to be discontinuous and spaced of about
449 140–160 km during the AMJ season (Fig.8e) but are more continuous for the ASO season
450 (Fig.8f). For the non-tidal simulation, the mean ZDF tends to be null in the ocean interior but
451 remains quite large ($> -0.2 \text{ }^\circ\text{C}\cdot\text{day}^{-1}$) in the thin surface layer during the two seasons (Fig.8g-
452 h).

453 Furthermore, it is worth to noting that along IT propagation's pathway, the maximum
454 of the ZDF follows the maxima of the baroclinic tidal energy dissipation (color shading in
455 Fig.2f). Thus, the dissipation of IT causes vertical mixing that enhances the cooling of the sea
456 surface. In addition, this temperature diffusion contributes to greater subsurface cooling within
457 the mixed-layer and warming in the deeper layers beneath the thermocline.

458 The seasonality of the stratification, highlighted above, could explain why the ZDF is
459 stronger along the slope and the near-coastal pathway B during the AMJ season (Fig.8a and
460 8e), and why ZDF is weaker along the slope, close to zero following B, and reinforce offshore
461 of A during the ASO season (Fig.8c and 8f). Previous studies have shown that stratification
462 influences the generation of internal tides and controls their modal distribution. Here we show
463 that stratification also plays a role on the fate of these internal tides, in this case on their
464 dissipation. The stratification could determine where IT dissipate their energy in the water
465 column, as mentioned by de Lavergne et al. (2020).

466 **IV.4.2. Advection of temperature**

467 The vertical (z -ADV) and the horizontal (h -ADV) terms of the temperature advection
468 tendency are averaged in the same depth-range as above for the two seasons.

469 **IV.4.2.a Vertical advection of Temperature**

470 z -ADV is almost null in these surface layers throughout the region (Fig.9a-d). For both
471 seasons, some weak extreme values are in the northwest on the plateau between 54°W – 50°W
472 and 3°N – 3°N and are for the same intensity between the two simulations with and without tides.
473 This result suggests that, overall, the tides fail to generate vertical temperature advection within
474 these surface layers, but deeper, z -ADV become higher. Vertical sections (Fig.9a-h) show an
475 intensification of z -ADV of about $\pm 0.8 \text{ }^\circ\text{C}\cdot\text{day}^{-1}$ located below the MLD and seems to be

476 centered around the thermocline, with a vertical extension from 20–200 m depth. z-ADV is
477 stronger in tidal simulation during both seasons (Fig.9e-f), and mainly presents sparse extrema
478 offshore (> 300 km) for the non-tidal simulation (Fig.9g-h). For the simulation with the tides,
479 z-ADV appears to be rather dominated by a cooling trend, with a marked hotspot on the slope
480 followed by other hotspots offshore. These extreme values are spaced about 120–150 km apart,
481 i.e., a mode-1 wavelength as for the baroclinic tidal energy dissipation (Fig.2f). Note that for
482 both simulations (Fig.10e-h), the extreme values are located within the narrow density (σ_θ)
483 contours [23.8 – 26.2 $\text{kg}\cdot\text{m}^{-3}$], i.e., within the pycnocline. The location of the extreme values of
484 z-ADV at the shelf break and along IT propagation's pathway and its negative sign suggest that
485 the diffusive part of the advection scheme might be the dominant process compared to nonlinear
486 effects.

487 **IV.4.2.b Horizontal advection of temperature**

488 Horizontal advection of temperature (h-ADV) is defined as the sum of the zonal (x-
489 ADV) and meridional (y-ADV) terms of temperature advection tendency. As for z-ADV, the
490 mean of h-ADV tends to be null over the entire domain in the surface layers for both seasons
491 in both simulations (Fig.10a-d). Nevertheless, some weak extreme values are in the northwest
492 of the plateau between 54°W – 50°W and 3°N – 3°N , that intensify during the ASO season in both
493 simulations, $\sim \pm 0.2$ $^\circ\text{C}\cdot\text{day}^{-1}$, Fig.10c and 10d for the tidal and non-tidal simulations
494 respectively. During AMJ, h-ADV is slightly stronger, ~ 0.1 $^\circ\text{C}\cdot\text{day}^{-1}$, around sites A and B in
495 the tidal simulation (Fig.10a), which appears to be related to IT generated along the slope. On
496 the other hand, the small difference between the two simulations in the surface layers shows
497 that the tides hardly generate h-ADV. Then, h-ADV hardly influence the cold-water tongue
498 observed over the surface SST during the ASO season (Fig.4d-f).

499 Along the vertical following A, h-ADV maxima remain essentially confined below the
500 mixed-layer depth, with much more intense values in the tidal simulation (Fig.10e-f) compared
501 to the non-tidal simulation (Fig.10g-h). h-ADV contributes to both warming and cooling of the
502 temperature of $\sim \pm 0.4$ $^\circ\text{C}\cdot\text{day}^{-1}$ from the slope to more than 500 km offshore. During both
503 seasons, the average vertical extension lies between the surface and 400 m depth for the tidal
504 simulation and a little less extended between 20–300 m depth for the non-tidal simulation. As
505 for z-ADV, h-ADV is also stronger within the pycnocline. For the tidal simulation, there is a
506 warming above the slope (0.4 $^\circ\text{C}\cdot\text{day}^{-1}$) reaching the surface in both seasons. This vertical
507 excursion is observed elsewhere for ZDF and z-ADV, and it is probably a marker of local
508 dissipation of IT at their generation site. This local dissipation clearly affects both advection

509 and vertical diffusion of the temperature but there are very low values along the slope when
510 averaging h-ADV or z-ADV between 2–20 m and much more strong values for the ZDF. This
511 means that the energy dissipated by internal tides is mostly transferred to mixing. In addition,
512 unlike ZDF and z-ADV, the (horizontal) location of h-ADV maxima mismatch IT dissipation
513 hotspots.

514 **IV.4.3. Heat budget balance**

515 Figure 10 shows the terms of the heat balance equation averaged below the MLD
516 between 60 and 400 m depth in a region around the IT trajectories emanating from A and B
517 between 40°W-48°W and 0°N-6°N. During the AMJ season, advection (ADV) dominates over
518 diffusion terms for both tidal (Fig.11a) and non-tidal (Fig.11b) simulations, while during the
519 ASO season, advection dominates only in tidal simulations (Fig.11c) and ZDF dominates in
520 non-tidal simulations (Fig.11d). We show here that advection terms dominate under the MLD,
521 while from the two sections above, in the tidal simulation, ZDF dominates the advection terms
522 at surface and within the mixed-layer and is the main contributor within the ocean processes to
523 explain SST changes. That vertical profile is probably the case in the real ocean since the tidal
524 simulation is more representative of reality.

525 **V. Discussion**

526 **V.1. On the role of advection in coastal upwelling**

527 To explain the cooling of the SST at the surface, Neto and da Silva (2014) indicated that
528 the steady flow of the NBC induces northward transport of water masses. This transport is in
529 turn offset by a vertical advection of cool water towards the surface. We demonstrate with our
530 model that the vertical advection hardly modifies the SST. But it is rather working below the
531 mixed layer (Fig.9e-h). The tides-induced vertical diffusion (mixing) extends from the mixed-
532 layer to deeper layers (Fig.8e-f). It is possible that the vertical mixing upwells to the surface the
533 water masses that are advected into the layers below the mixed layer. The temperature change
534 at the surface and within the mixed-layer can then be influenced to first order by (i) the vertical
535 diffusion of temperature and (ii) a cross effect between the latter and the advection (vertical and
536 horizontal) of temperature that mainly takes place below MLD.

537 **V.2. The mode-1 wavelenth in the vertical terms of the heat budget equation**

538 Along the vertical and toward the open ocean, both ZDF and z-ADV tendencies are found
539 to have a wave-like structure. For z-ADV, patches are spaced apart by about 120–150 km and

540 140–160 km for the AMJ and ASO seasons respectively. Whilst for z-ADV, this wavelength is
541 about 140–160 km during the AMJ season and more continuous patches for the ASO season.
542 The wavelength ranges found in heat budget terms are slightly wider (+ 10–20 km, for z-ADV
543 in ASO season and for ZDF) than the purely dynamic tidal coherent wavelength (\sim 120–150
544 km, see section III.1). The difference can be understood as the effect of incoherent IT that are
545 not captured by the harmonic analysis because they are deviated or diffracted by the currents
546 and eddies, and for which dissipation occurs around where coherent IT dissipate. Hence, the
547 total (coherent + incoherent) dissipation pattern of IT could be wider than in Figure 2f. When
548 integrating heat budget terms over the season, this cumulative effect is considered and therefore
549 leads to diffusive patterns and wider wavelength. This diffusive effect increases during the ASO
550 season when both background circulation and eddy activity increase.

551 Recently, de Macedo et al. (2023) gave a detailed description of internal solitary waves
552 (ISW) in this region from remote sensing data. These ISW originate from instabilities and
553 energy loss or dissipation of IT radiating from the slope, mainly along the pathways A and B
554 (Magalhaes et al., 2016). The first have shown that inter-packet distance of ISW corresponds
555 to mode-1 wavelength. IT dissipation and deeper heat budget terms patches of our simulations
556 are colocalized horizontally with observed ISW packets. This means that our model well
557 reproduces the location of IT dissipation.

558 **V.3. Tidal impact at the mouth of the Amazon River and on the southern** 559 **shelf: two main competitive processes**

560 In the simulation without the tides, there is a strong along-coast current exiting
561 northwesterly the mouth of the Amazon River (e.g., Ruault et al., 2020) with an average
562 intensity $> 0.5 \text{ m}\cdot\text{s}^{-1}$ in the first 50 meters for both seasons (Fig.12a-b). When including the tides
563 in the model, the latter study showed that there is an increase in the vertical mixing in the water
564 column due to stratified-shear flow instability, which weakens and deflects the along-coast
565 current north-eastwards at the mouth of the Amazon River (Fig.12c-d) and favours cross-shore
566 export of water. We can therefore establish that there are at least two processes at work: (i)
567 vertical mixing and (ii) horizontal transport, backed respectively by ZDF and h-ADV. We then
568 looked at the latter two processes along the vertical following the cross-shore transect (C-S)
569 defined in Figure 10b. Hereinafter, “inner mouth” refers to the part of the transect before 200
570 km, whereas “outer shelf” refers to the part beyond.

571 During the AMJ season, in the inner mouth, river flow dominates and tide-induced vertical
572 mixing in the narrow water column leads to warming and deepening of the thermocline

573 (Fig.13a-b). On the outer shelf, this mixing in the thicker water column leads to cooling above
574 the thermocline and warming below (Fig.13a), which in turn extends across the shelf and along
575 the pathways of IT as shown in section IV.4.1 (see Fig.8a and 8e). At the same time, the SST
576 on the shelf is somewhat homogeneous (see Fig.4a-c) and solar radiation is lower than 190
577 W.m^{-2} (not shown). As a result, waters of similar temperature are advected horizontally, i.e., h-
578 ADV is low (Fig.13b). Thus, for the first season, vertical mixing seems to be the dominant
579 process explaining the average negative SST anomaly on the plateau.

580 For the second season, solar radiation on the shelf rose sharply with an average value of 60
581 W.m^{-2} compared with the previous season (Fig.13c) and the average depth of the thermocline
582 deepens offshore (Fig.13d and 13e). In this season, mixing leads to warming in the thin surface
583 layer ($< 2\text{m}$, Fig.13d). The NBC is stronger and can influence transport over the shelf (Prestes
584 et al., 2018) and the small mean tidal residual transport should also be considered (Bessières et
585 al., 2008). The region is more dynamic, and waters of distinct temperatures are advected over
586 the shelf. Consequently, h-ADV is stronger and positive (Fig.13e) and then plays a greater role
587 in the fate of SST. For this season, ZDF and h-ADV add to explain the positive SST anomaly
588 on the shelf. In addition, from AMJ to ASO, we noted the deepening of the thermocline depth
589 on the outer shelf. This was previously highlighted by Silva et al. (2005) from REVIZEE
590 (Recursos Vivos da Zona Econômica Exclusiva) campaign data and is a further contribution to
591 the validation of our simulations.

592 **V.4. Mixing in the NBC retroflection area**

593 To the north-west of the domain [3°N – 9°N and 53°W – 45°W], in the surface layers (2–
594 20m), eddy-like or circular patterns exist in ZDF during the ASO season for the simulation
595 including tides (Fig.8c). NBC intensifies and retroflects, and strong eddy activity takes place
596 there during ASO. We can assume that this intense mesoscale activity influences the mixing
597 and subsequent temperature diffusion. However, it is not yet clear how these mesoscale features
598 produce mixing. Fronts exist in such region and are associated with high horizontal temperature
599 gradient (∇T) and significant vertical mixing (see Chapman et al., 2020). We therefore
600 examined the mean ∇T in the same depth range (2–20m) as ZDF (Fig.8a-d). During the AMJ
601 season, it is on average equal to $4 \cdot 10^{-2} \text{ }^{\circ}\text{C}/10 \text{ km}$. As expected, it does not reveal any circular
602 fronts for the two simulations (Fig.14a-b) since mesoscale activity is low. Then ∇T increases
603 during the ASO season [$> 5 \cdot 10^{-2} \text{ }^{\circ}\text{C}/10 \text{ km}$] in the north-west and exhibits circular and
604 filamentary fronts in both the non-tidal (Fig.14c) and tidal (Fig.14d) simulations. Therefore,
605 one would expect to see the same circular patterns in the ZDF for both simulations, this is not

606 actually the case (see Fig.8c and 8d). Another hypothesis is that these circular patterns could be
607 originated from the interaction between IT and near-inertial oscillations, which can enhance
608 mixing and vertical transport processes in the ocean. But quantifying this interaction requires
609 further analysis and is beyond the scope this study.

610 VI. Summary

611 In this paper, we used twin oceanic simulations (with and without tides) from a realistic
612 model to explore the impact of internal tidal waves (IT) on temperature and associated
613 processes. The impact on the atmosphere-to-ocean net heat fluxes is also covered.

614 The AMAZON36 configuration can reproduce the generation of IT from two most
615 energetic sites A and B, in good agreement with previous studies. The model well reproduces
616 their local, on-shelf, and offshore dissipation with two beams of mode-1 propagation (120–150
617 km). This dissipation occurs less than 300 km from the slope. Then, we assess the ability of the
618 model to reproduce temperature structure. The simulations including tides is in better agreement
619 with SST observations and better reproduce water mass properties along the vertical.

620 Our analyses were based on three years (2013-2015) of data averaged over two seasons,
621 AMJ (April-May-June) and ASO (August-September-October). That are highly contrasted in
622 terms of stratification, background circulation and EKE. Results show that for both seasons, the
623 tides create SST cooling of about 0.3 °C in the plume of the Amazon offshore and along the
624 paths of internal tides. During ASO, the cold waters of the ACT enter our domain along the
625 coast and are affected by the tides. This enhances that seasonal upwelling and leads to cooler
626 SST. Over the Amazon shelf, the tides induce the same magnitude cooling in AMJ and in turn
627 induce an opposite anomaly (warming) in ASO. These cooling/warming are responsible in the
628 same location for an increase/decrease in the net heat flux from the atmosphere to the ocean
629 (Q_t). However, the overall effect of the tides is an increase of Q_t , which lies between [33.2% –
630 7.4%] from AMJ to ASO and is larger than in other regions. When increasing the atmosphere-
631 to-ocean net heat flux in such large atmospheric convection region, marked by the ITCZ, the
632 tides can reduce the cloud convection into the atmosphere (Koch-Larrouy et al., 2010).
633 Therefore, this tidal effect on the climate might have a key importance for the future, taking the
634 climate change into account (Yadidya and Rao, 2022).

635 In the subsurface, above the thermocline (< 120 m), the tides induce a stronger cooling
636 (~ 1.2 °C) than at the surface. And an associated warming of the same magnitude under the
637 thermocline (> 120 – 300 m). We analyzed the terms of the heat budget equation to identify to

638 processes that modify the temperature. We found that the vertical diffusion of temperature
639 (ZDF) is mainly caused by the dissipation of the tides. Horizontal (h-ADV) and vertical (z-
640 ADV) advection can be driven by non-tidal processes but increase when including the tides in
641 the model.

642 Over the shelf, barotropic tidal mixing increases ZDF ($> |-0.4| \text{ }^\circ\text{C}\cdot\text{day}^{-1}$) and explain the
643 cooling of the water column in AMJ season. During the second season, it combines with h-
644 ADV and to cause a warming. Off the shelf, the (baroclinic) mixing takes place from the slope
645 to about 700 km following the path A, and 300 km following the path B. That mixing induces
646 ZDF with values of about $-0.4 \text{ }^\circ\text{C}\cdot\text{day}^{-1}$, which is the main process in the upper layer above the
647 mixed layer but could combine with advection terms (z-ADV and h-ADV) to explain the
648 temperature changes below the mixed layer. Some ZDF and z-ADV patches are colocalized
649 with dissipation hotspots along the trajectory of IT.

650 This study highlights the key role of internal tides in creating intensified mixing which
651 is important for temperature structure. Other analysis we performed with our simulations show
652 that this mixing can also impact salinity. Furthermore, they might be seen as a source of nutrient
653 uptake at tidal frequency and can have an impact on the spatial distribution of phytoplankton
654 and zooplankton, and therefore on the entire food chain (Sharples et al., 2007, 2009; Xu et al.,
655 2020). These other impacts can be studied through a combined model-in situ data approach.
656 Long-term PIRATA (PredIction and Research moored Array in the Tropical Atlantic) mooring
657 data are available for this goal (Bourlès et al., 2019). In addition, recently in late 2021, the
658 AMAZOn MIXing (“AMAZOMIX”) campaign took place in this region. Among other things,
659 this campaign was dedicated to internal tides. It provided a huge set of data, with the aim of
660 understanding their impact on marine ecosystems (see details in [https://en.ird.fr/amazomix-](https://en.ird.fr/amazomix-campaign-impact-physical-processes-marine-ecosystem-mouth-amazon)
661 [campaign-impact-physical-processes-marine-ecosystem-mouth-amazon](https://en.ird.fr/amazomix-campaign-impact-physical-processes-marine-ecosystem-mouth-amazon)). In the meantime, a
662 coupled physical/biogeochemistry simulation (NEMO/PISCES) is being analyzed and will
663 begin to answer these crucial questions.

664 Finally, we focused hereabove on describing the impacts of tides on a seasonal scale. A
665 companion paper will then analyze the variability of temperature at tidal and subtidal scales
666 using our model simulations and two observational data.

667

668 **Data availability statements**

669 The 2020’s release of GEBCO bathymetry is publicly available online through:
670 https://www.gebco.net/data_and_products/gridded_bathymetry_data/gebco_2020/. The TMI

671 SST v7.1 data are publicly available online from the REMSS platform:
672 <https://www.remss.com/missions/tmi/>, was accessed on 27 June 2022. WOA2018 climatology
673 is publicly available online at: <https://www.ncei.noaa.gov/access/world-ocean-atlas-2018/>, was
674 accessed on 27 June 2022. The model simulations are available upon request by contacting the
675 corresponding author.

676 **Authors contributions**

677 Funding acquisition, AKL; Conceptualization and methodology, FA, AKL and ID.
678 Numerical simulations, GM and FA. Formal analysis, FA; FA prepared the paper with
679 contribution from all co-authors.

680 **Competing interests**

681 The authors declare that they have no conflict of interest.

682 **Funding**

683 This work is part of the PhD Thesis of FA, cofounded by Institut de Recherche pour le
684 Développement (IRD) and Mercator Ocean International (MOi), under the supervision of AKL
685 and ID. The numerical simulations were founded by CNRS/CNES/IRD via the projects
686 A0080111357 and A0130111357 and were performed thank to “Jean-Zay”, the
687 CNRS/GENCI/IDRIS platform for modelling and computing.

688 **Acknowledgments**

689 The authors would like to thank the Editorial team for their availability, and the two
690 reviewers Clément Vic and Nicolas Grissouard for their valuable comments, which enhanced
691 the quality of the present work.

692

693 **References**

- 694 Aguedjou, H.M.A., Chaigneau, A., Dadou, I., Morel, Y., Pegliasco, C., Da-Allada, C.Y.,
695 Baloïtcha, E., 2021. What Can We Learn From Observed Temperature and Salinity
696 Isopycnal Anomalies at Eddy Generation Sites? Application in the Tropical Atlantic
697 Ocean. *J. Geophys. Res. Oceans* 126, e2021JC017630.
698 <https://doi.org/10.1029/2021JC017630>
- 699 Aguedjou, H.M.A., Dadou, I., Chaigneau, A., Morel, Y., Alory, G., 2019. Eddies in the Tropical
700 Atlantic Ocean and Their Seasonal Variability. *Geophys. Res. Lett.* 46, 12156–12164.
701 <https://doi.org/10.1029/2019GL083925>
- 702 Archer, D., Martin, P., Buffett, B., Brovkin, V., Rahmstorf, S., Ganopolski, A., 2004. The
703 importance of ocean temperature to global biogeochemistry. *Earth Planet. Sci. Lett.* 222,
704 333–348. <https://doi.org/10.1016/j.epsl.2004.03.011>

705 Baines, P.G., 1982. On internal tide generation models. *Deep Sea Res. Part Oceanogr. Res. Pap.*
706 29, 307–338. [https://doi.org/10.1016/0198-0149\(82\)90098-X](https://doi.org/10.1016/0198-0149(82)90098-X)

707 Barbot, S., Lyard, F., Tchilibou, M., Carrere, L., 2021. Background stratification impacts on
708 internal tide generation and abyssal propagation in the western equatorial Atlantic and
709 the Bay of Biscay. *Ocean Sci.* 17, 1563–1583. <https://doi.org/10.5194/os-17-1563-2021>

710 Barton, E.D., Inall, M.E., Sherwin, T.J., Torres, R., 2001. Vertical structure, turbulent mixing
711 and fluxes during Lagrangian observations of an upwelling filament system off
712 Northwest Iberia. *Prog. Oceanogr., Lagrangian studies of the Iberian upwelling system*
713 51, 249–267. [https://doi.org/10.1016/S0079-6611\(01\)00069-6](https://doi.org/10.1016/S0079-6611(01)00069-6)

714 Beardsley, R.C., Candela, J., Limeburner, R., Geyer, W.R., Lentz, S.J., Castro, B.M.,
715 Cacchione, D., Carneiro, N., 1995. The M2 tide on the Amazon Shelf. *J. Geophys. Res.*
716 *Oceans* 100, 2283–2319. <https://doi.org/10.1029/94JC01688>

717 Bessières, L., 2007. Impact des marées sur la circulation générale océanique dans une
718 perspective climatique (phdthesis). Université Paul Sabatier - Toulouse III.

719 Bessières, L., Madec, G., Lyard, F., 2008. Global tidal residual mean circulation: Does it affect
720 a climate OGCM? *Geophys. Res. Lett.* 35. <https://doi.org/10.1029/2007GL032644>

721 Bourlès, B., Araujo, M., McPhaden, M.J., Brandt, P., Foltz, G.R., Lumpkin, R., Giordani, H.,
722 Hernandez, F., Lefèvre, N., Nobre, P., Campos, E., Saravanan, R., Trotte-Duhà, J.,
723 Dengler, M., Hahn, J., Hummels, R., Lübbecke, J.F., Rouault, M., Cotrim, L., Sutton,
724 A., Jochum, M., Perez, R.C., 2019. PIRATA: A Sustained Observing System for
725 Tropical Atlantic Climate Research and Forecasting. *Earth Space Sci.* 6, 577–616.
726 <https://doi.org/10.1029/2018EA000428>

727 Bourles, B., Molinari, R.L., Johns, E., Wilson, W.D., Leaman, K.D., 1999. Upper layer currents
728 in the western tropical North Atlantic (1989–1991). *J. Geophys. Res. Oceans* 104, 1361–
729 1375. <https://doi.org/10.1029/1998JC900025>

730 Buijsman, M.C., Arbic, B.K., Richman, J.G., Shriver, J.F., Wallcraft, A.J., Zamudio, L., 2017.
731 Semidiurnal internal tide incoherence in the equatorial Pacific. *J. Geophys. Res. Oceans*
732 122, 5286–5305. <https://doi.org/10.1002/2016JC012590>

733 C., Le Provost, Florent, Lyard, 1997. Energetics of the M2 barotropic ocean tides: an estimate
734 of bottom friction dissipation from a hydrodynamic model - ScienceDirect. *Prog.*
735 *Oceanogr.* 37–52.

736 Chapman, C.C., Lea, M.-A., Meyer, A., Sallée, J.-B., Hindell, M., 2020. Defining Southern
737 Ocean fronts and their influence on biological and physical processes in a changing
738 climate. *Nat. Clim. Change* 10, 209–219. <https://doi.org/10.1038/s41558-020-0705-4>

739 Clayson, C.A., Bogdanoff, A.S., 2013. The Effect of Diurnal Sea Surface Temperature
740 Warming on Climatological Air–Sea Fluxes. *Am. Meteorol. Soc.*

741 Collins, M., An, S.-I., Cai, W., Ganachaud, A., Guilyardi, E., Jin, F.-F., Jochum, M., Lengaigne,
742 M., Power, S., Timmermann, A., Vecchi, G., Wittenberg, A., 2010. The impact of global
743 warming on the tropical Pacific Ocean and El Niño. *Nat. Geosci.* 3, 391–397.
744 <https://doi.org/10.1038/ngeo868>

745 de Lavergne, C., Vic, C., Madec, G., Roquet, F., Waterhouse, A.F., Whalen, C.B., Cuypers, Y.,
746 Bouruet-Aubertot, P., Ferron, B., Hibiya, T., 2020. A Parameterization of Local and
747 Remote Tidal Mixing. *J. Adv. Model. Earth Syst.* 12, e2020MS002065.
748 <https://doi.org/10.1029/2020MS002065>

749 de Macedo, C.R., Koch-Larrouy, A., da Silva, J.C.B., Magalhães, J.M., Lentini, C.A.D., Tran,
750 T.K., Rosa, M.C.B., Vantrepotte, V., 2023. Spatial and temporal variability of mode-1
751 and mode-2 internal solitary waves from MODIS/TERRA sunglint off the Amazon shelf
752 (preprint). *Remote Sensing/Internal waves/Surface/Deep Seas: Equatorial Ocean/Other.*
753 <https://doi.org/10.5194/egusphere-2022-1482>

754 Didden, N., Schott, F., 1993. Eddies in the North Brazil Current retroflexion region observed
755 by Geosat altimetry. *J. Geophys. Res. Oceans* 98, 20121–20131.
756 <https://doi.org/10.1029/93JC01184>

757 Dong, S., Sprintall, J., Gille, S.T., Talley, L., 2008. Southern Ocean mixed-layer depth from
758 Argo float profiles. *J. Geophys. Res. Oceans* 113.
759 <https://doi.org/10.1029/2006JC004051>

760 Dunphy, M., Lamb, K.G., 2014. Focusing and vertical mode scattering of the first mode internal
761 tide by mesoscale eddy interaction. *J. Geophys. Res. Oceans* 119, 523–536.
762 <https://doi.org/10.1002/2013JC009293>

763 Egbert, G.D., Ray, R.D., 2000. Significant dissipation of tidal energy in the deep ocean inferred
764 from satellite altimeter data. *Nature* 405, 775–778. <https://doi.org/10.1038/35015531>

765 Fassoni-Andrade, A.C., Durand, F., Azevedo, A., Bertin, X., Santos, L.G., Khan, J.U., Testut,
766 L., Moreira, D.M., 2023. Seasonal to interannual variability of the tide in the Amazon
767 estuary. *Cont. Shelf Res.* 255, 104945. <https://doi.org/10.1016/j.csr.2023.104945>

768 Fontes, R.F.C., Castro, B.M., Beardsley, R.C., 2008. Numerical study of circulation on the inner
769 Amazon Shelf. *Ocean Dyn.* 58, 187–198. <https://doi.org/10.1007/s10236-008-0139-4>

770 Gabioux, M., Vinzon, S.B., Paiva, A.M., 2005. Tidal propagation over fluid mud layers on the
771 Amazon shelf. *Cont. Shelf Res.* 25, 113–125. <https://doi.org/10.1016/j.csr.2004.09.001>

772 Garzoli, S.L., Field, A., Yao, Q., 2003. North Brazil Current rings and the variability in the
773 latitude of retroflexion, in: Goni, G.J., Malanotte-Rizzoli, P. (Eds.), Elsevier
774 Oceanography Series, Interhemispheric Water Exchange in the Atlantic Ocean.
775 Elsevier, pp. 357–373. [https://doi.org/10.1016/S0422-9894\(03\)80154-X](https://doi.org/10.1016/S0422-9894(03)80154-X)

776 Gévaudan, M., Durand, F., Jouanno, J., 2022. Influence of the Amazon-Orinoco Discharge
777 Interannual Variability on the Western Tropical Atlantic Salinity and Temperature. *J.*
778 *Geophys. Res. Oceans* 127, e2022JC018495. <https://doi.org/10.1029/2022JC018495>

779 Hernandez, O., Jouanno, J., Durand, F., 2016. Do the Amazon and Orinoco freshwater plumes
780 really matter for hurricane-induced ocean surface cooling? *J. Geophys. Res. Oceans*
781 121, 2119–2141. <https://doi.org/10.1002/2015JC011021>

782 Hernandez, O., Jouanno, J., Echevin, V., Aumont, O., 2017. Modification of sea surface
783 temperature by chlorophyll concentration in the Atlantic upwelling systems. *J. Geophys.*
784 *Res. Oceans* 122, 5367–5389. <https://doi.org/10.1002/2016JC012330>

785 Hersbach, H., Bell, B., Berrisford, P., Hirahara, S., Horányi, A., Muñoz-Sabater, J., Nicolas, J.,
786 Peubey, C., Radu, R., Schepers, D., Simmons, A., Soci, C., Abdalla, S., Abellan, X.,
787 Balsamo, G., Bechtold, P., Biavati, G., Bidlot, J., Bonavita, M., De Chiara, G.,
788 Dahlgren, P., Dee, D., Diamantakis, M., Dragani, R., Flemming, J., Forbes, R., Fuentes,
789 M., Geer, A., Haimberger, L., Healy, S., Hogan, R.J., Hólm, E., Janisková, M., Keeley,
790 S., Laloyaux, P., Lopez, P., Lupu, C., Radnoti, G., de Rosnay, P., Rozum, I., Vamborg,
791 F., Villaume, S., Thépaut, J.-N., 2020. The ERA5 global reanalysis. *Q. J. R. Meteorol.*
792 *Soc.* 146, 1999–2049. <https://doi.org/10.1002/qj.3803>

793 Jayakrishnan, P.R., Babu, C.A., 2013. Study of the Oceanic Heat Budget Components over the
794 Arabian Sea during the Formation and Evolution of Super Cyclone, Gonu 2013.
795 <https://doi.org/10.4236/acs.2013.33030>

796 Jithin, A.K., Francis, P.A., 2020. Role of internal tide mixing in keeping the deep Andaman Sea
797 warmer than the Bay of Bengal. *Sci. Rep.* 10, 11982. <https://doi.org/10.1038/s41598-020-68708-6>

799 Johns, W.E., Lee, T.N., Beardsley, R.C., Candela, J., Limeburner, R., Castro, B., 1998. Annual
800 Cycle and Variability of the North Brazil Current. *J. Phys. Oceanogr.* 28, 103–128.
801 [https://doi.org/10.1175/1520-0485\(1998\)028<0103:ACAVOT>2.0.CO;2](https://doi.org/10.1175/1520-0485(1998)028<0103:ACAVOT>2.0.CO;2)

802 Johns, W.E., Lee, T.N., Schott, F.A., Zantopp, R.J., Evans, R.H., 1990. The North Brazil
803 Current retroflexion: Seasonal structure and eddy variability. *J. Geophys. Res. Oceans*
804 95, 22103–22120. <https://doi.org/10.1029/JC095iC12p22103>

805 Jouanno, J., Marin, F., du Penhoat, Y., Sheinbaum, J., Molines, J.-M., 2011. Seasonal heat
806 balance in the upper 100 m of the equatorial Atlantic Ocean. *J. Geophys. Res. Oceans*
807 116. <https://doi.org/10.1029/2010JC006912>

808 Kara, A.B., Rochford, P.A., Hurlburt, H.E., 2003. Mixed layer depth variability over the global
809 ocean. *J. Geophys. Res. Oceans* 108. <https://doi.org/10.1029/2000JC000736>

810 Kelly, S.M., Nash, J.D., Kunze, E., 2010. Internal-tide energy over topography. *J. Geophys.*
811 *Res. Oceans* 115. <https://doi.org/10.1029/2009JC005618>

812 Koch-Larrouy, A., Atmadipoera, A., van Beek, P., Madec, G., Aucan, J., Lyard, F., Grelet, J.,
813 Souhaut, M., 2015. Estimates of tidal mixing in the Indonesian archipelago from
814 multidisciplinary INDOMIX in-situ data. *Deep Sea Res. Part Oceanogr. Res. Pap.* 106,
815 136–153. <https://doi.org/10.1016/j.dsr.2015.09.007>

816 Koch-Larrouy, A., Lengaigne, M., Terray, P., Madec, G., Masson, S., 2010. Tidal mixing in the
817 Indonesian Seas and its effect on the tropical climate system. *Clim. Dyn.* 34, 891–904.
818 <https://doi.org/10.1007/s00382-009-0642-4>

819 Koch-Larrouy, A., Madec, G., Bouruet-Aubertot, P., Gerkema, T., Bessières, L., Molcard, R.,
820 2007. On the transformation of Pacific Water into Indonesian Throughflow Water by
821 internal tidal mixing. *Geophys. Res. Lett.* 34. <https://doi.org/10.1029/2006GL028405>

822 Koch-Larrouy, A., Madec, G., Iudicone, D., Atmadipoera, A., Molcard, R., 2008. Physical
823 processes contributing to the water mass transformation of the Indonesian Throughflow.
824 *Ocean Dyn.* 58, 275–288. <https://doi.org/10.1007/s10236-008-0154-5>

825 Kosuth, P., Callède, J., Laraque, A., Filizola, N., Guyot, J.L., Seyler, P., Fritsch, J.M.,
826 Guimarães, V., 2009. Sea-tide effects on flows in the lower reaches of the Amazon
827 River. *Hydrol. Process.* 23, 3141–3150. <https://doi.org/10.1002/hyp.7387>

828 Kunze, E., MacKay, C., McPhee-Shaw, E.E., Morrice, K., Girton, J.B., Terker, S.R., 2012.
829 Turbulent Mixing and Exchange with Interior Waters on Sloping Boundaries. *J. Phys.*
830 *Oceanogr.* 42, 910–927. <https://doi.org/10.1175/JPO-D-11-075.1>

831 Lambeck, K., Runcorn, S.K., 1977. Tidal dissipation in the oceans: astronomical, geophysical
832 and oceanographic consequences. *Philos. Trans. R. Soc. Lond. Ser. Math. Phys. Sci.*
833 287, 545–594. <https://doi.org/10.1098/rsta.1977.0159>

834 Lascaratos, A., 1993. Estimation of deep and intermediate water mass formation rates in the
835 Mediterranean Sea. *Deep Sea Res. Part II Top. Stud. Oceanogr.* 40, 1327–1332.
836 [https://doi.org/10.1016/0967-0645\(93\)90072-U](https://doi.org/10.1016/0967-0645(93)90072-U)

837 Laurent, L.S., Garrett, C., 2002. The Role of Internal Tides in Mixing the Deep Ocean. *J. Phys.*
838 *Oceanogr.* 32, 2882–2899. [https://doi.org/10.1175/1520-0485\(2002\)032<2882:TROITI>2.0.CO;2](https://doi.org/10.1175/1520-0485(2002)032<2882:TROITI>2.0.CO;2)

840 Leclair, M., Madec, G., 2009. A conservative leapfrog time stepping method. *Ocean Model.*
841 30, 88–94. <https://doi.org/10.1016/j.ocemod.2009.06.006>

842 Lellouche, J.-M., Greiner, E., Le Galloudec, O., Garric, G., Regnier, C., Drevillon, M.,
843 Benkiran, M., Testut, C.-E., Bourdalle-Badie, R., Gasparin, F., Hernandez, O., Levier,
844 B., Drillet, Y., Remy, E., Le Traon, P.-Y., 2018. Recent updates to the Copernicus
845 Marine Service global ocean monitoring and forecasting real-time 1/12° high-resolution
846 system. *Ocean Sci.* 14, 1093–1126. <https://doi.org/10.5194/os-14-1093-2018>

847 Lentini, C.A.D., Magalhães, J.M., da Silva, J.C.B., Lorenzetti, J.A., 2016. Transcritical Flow
848 and Generation of Internal Solitary Waves off the Amazon River: Synthetic Aperture
849 Radar Observations and Interpretation. *Oceanography* 29, 187–195.

- 850 Lentz, S.J., Limeburner, R., 1995. The Amazon River Plume during AMASSEDs: Spatial
851 characteristics and salinity variability. *J. Geophys. Res. Oceans* 100, 2355–2375.
852 <https://doi.org/10.1029/94JC01411>
- 853 Li, C., Zhou, W., Jia, X., Wang, X., 2006. Decadal/interdecadal variations of the ocean
854 temperature and its impacts on climate. *Adv. Atmospheric Sci.* 23, 964–981.
855 <https://doi.org/10.1007/s00376-006-0964-7>
- 856 Li, Y., Curchitser, E.N., Wang, J., Peng, S., 2020. Tidal Effects on the Surface Water Cooling
857 Northeast of Hainan Island, South China Sea. *J. Geophys. Res. Oceans* 125,
858 e2019JC016016. <https://doi.org/10.1029/2019JC016016>
- 859 Lyard, F.H., Allain, D.J., Cancet, M., Carrère, L., Picot, N., 2021. FES2014 global ocean tide
860 atlas: design and performance. *Ocean Sci.* 17, 615–649. [https://doi.org/10.5194/os-17-](https://doi.org/10.5194/os-17-615-2021)
861 [615-2021](https://doi.org/10.5194/os-17-615-2021)
- 862 Magalhaes, J.M., da Silva, J.C.B., Buijsman, M.C., Garcia, C. a. E., 2016. Effect of the North
863 Equatorial Counter Current on the generation and propagation of internal solitary waves
864 off the Amazon shelf (SAR observations). *Ocean Sci.* 12, 243–255.
865 <https://doi.org/10.5194/os-12-243-2016>
- 866 Mei, W., Xie, S.-P., Primeau, F., McWilliams, J.C., Pasquero, C., 2015. Northwestern Pacific
867 typhoon intensity controlled by changes in ocean temperatures. *Sci. Adv.* 1, e1500014.
868 <https://doi.org/10.1126/sciadv.1500014>
- 869 Moisan, J.R., Niiler, P.P., 1998. The Seasonal Heat Budget of the North Pacific: Net Heat Flux
870 and Heat Storage Rates (1950–1990). *J. Phys. Oceanogr.* 28, 401–421.
871 [https://doi.org/10.1175/1520-0485\(1998\)028<0401:TSHBOT>2.0.CO;2](https://doi.org/10.1175/1520-0485(1998)028<0401:TSHBOT>2.0.CO;2)
- 872 Muller-Karger, F.E., McClain, C.R., Richardson, P.L., 1988. The dispersal of the Amazon's
873 water. *Nature* 333, 56–59. <https://doi.org/10.1038/333056a0>
- 874 Munk, W., Wunsch, C., 1998. Abyssal recipes II: energetics of tidal and wind mixing. *Deep*
875 *Sea Res. Part Oceanogr. Res. Pap.* 45, 1977–2010. [https://doi.org/10.1016/S0967-](https://doi.org/10.1016/S0967-0637(98)00070-3)
876 [0637\(98\)00070-3](https://doi.org/10.1016/S0967-0637(98)00070-3)
- 877 Nagai, T., Hibiya, T., 2015. Internal tides and associated vertical mixing in the Indonesian
878 Archipelago. *J. Geophys. Res. Oceans* 120, 3373–3390.
879 <https://doi.org/10.1002/2014JC010592>
- 880 Madec, G., Bourdallé-Badie, R., Chanut, J., Clementi, E., Coward, A., Ethé, C., Iovino, D., Lea,
881 D., Lévy, C., Lovato, T., Martin, N., Masson, S., Mocavero, S., Rousset, C., Storkey,
882 D., Vancoppenolle, M., Müeller, S., Nurser, G., Bell, M., & Samson, G., 2019. NEMO
883 ocean engine. In *Notes du Pôle de modélisation de l'Institut Pierre-Simon Laplace*
884 (IPSL) (v4.0, Numéro 27). Zenodo. <https://doi.org/10.5281/zenodo.3878122>
- 885 Neto, A.V.N., da Silva, A.C., 2014. Seawater temperature changes associated with the North
886 Brazil current dynamics. *Ocean Dyn.* 64, 13–27. [https://doi.org/10.1007/s10236-013-](https://doi.org/10.1007/s10236-013-0667-4)
887 [0667-4](https://doi.org/10.1007/s10236-013-0667-4)
- 888 Niwa, Y., Hibiya, T., 2011. Estimation of baroclinic tide energy available for deep ocean mixing
889 based on three-dimensional global numerical simulations. *J. Oceanogr.* 67, 493–502.
890 <https://doi.org/10.1007/s10872-011-0052-1>
- 891 Nugroho, D., Koch-Larrouy, A., Gaspar, P., Lyard, F., Reffray, G., Tranchant, B., 2018.
892 Modelling explicit tides in the Indonesian seas: An important process for surface sea
893 water properties. *Mar. Pollut. Bull., Special Issue: Indonesia seas management* 131, 7–
894 18. <https://doi.org/10.1016/j.marpolbul.2017.06.033>
- 895 Peng, S., Liao, J., Wang, X., Liu, Z., Liu, Y., Zhu, Y., Li, B., Khokiattiwong, S., Yu, W., 2021.
896 Energetics Based Estimation of the Diapycnal Mixing Induced by Internal Tides in the
897 Andaman Sea. *J. Geophys. Res. Oceans* 126. <https://doi.org/10.1029/2020JC016521>

898 Prestes, Y.O., Silva, A.C. da, Jeandel, C., 2018. Amazon water lenses and the influence of the
899 North Brazil Current on the continental shelf. *Cont. Shelf Res.* 160, 36–48.
900 <https://doi.org/10.1016/j.csr.2018.04.002>

901 Richardson, P.L., Hufford, G.E., Limeburner, R., Brown, W.S., 1994. North Brazil Current
902 retroflection eddies. *J. Geophys. Res. Oceans* 99, 5081–5093.
903 <https://doi.org/10.1029/93JC03486>

904 Rosenthal, Y., Boyle, E.A., Slowey, N., 1997. Temperature control on the incorporation of
905 magnesium, strontium, fluorine, and cadmium into benthic foraminiferal shells from
906 Little Bahama Bank: Prospects for thermocline paleoceanography. *Geochim.
907 Cosmochim. Acta* 61, 3633–3643. [https://doi.org/10.1016/S0016-7037\(97\)00181-6](https://doi.org/10.1016/S0016-7037(97)00181-6)

908 Ruault, V., Jouanno, J., Durand, F., Chanut, J., Benshila, R., 2020. Role of the Tide on the
909 Structure of the Amazon Plume: A Numerical Modeling Approach. *J. Geophys. Res.
910 Oceans* 125, e2019JC015495. <https://doi.org/10.1029/2019JC015495>

911 Salamena, G.G., Whinney, J.C., Heron, S.F., Ridd, P.V., 2021. Internal tidal waves and deep-
912 water renewal in a tropical fjord: Lessons from Ambon Bay, eastern Indonesia. *Estuar.
913 Coast. Shelf Sci.* 253, 107291. <https://doi.org/10.1016/j.ecss.2021.107291>

914 Schott, F.A., Dengler, M., Brandt, P., Affler, K., Fischer, J., Bourlès, B., Gouriou, Y., Molinari,
915 R.L., Rhein, M., 2003. The zonal currents and transports at 35°W in the tropical
916 Atlantic. *Geophys. Res. Lett.* 30. <https://doi.org/10.1029/2002GL016849>

917 Sharples, J., Moore, C.M., Hickman, A.E., Holligan, P.M., Tweddle, J.F., Palmer, M.R.,
918 Simpson, J.H., 2009. Internal tidal mixing as a control on continental margin
919 ecosystems. *Geophys. Res. Lett.* 36. <https://doi.org/10.1029/2009GL040683>

920 Sharples, J., Tweddle, J.F., Green, J.A.M., Palmer, M.R., Kim, Y.-N., Hickman, A.E., Holligan,
921 P.M., Moore, C.M., Rippeth, T.P., Simpson, J.H., Krivtsov, V., 2007. Spring-neap
922 modulation of internal tide mixing and vertical nitrate fluxes at a shelf edge in summer.
923 *Limnol. Oceanogr.* 52, 1735–1747. <https://doi.org/10.4319/lo.2007.52.5.1735>

924 Silva, A., Araujo, M., Medeiros, C., Silva, M., Bourles, B., 2005. Seasonal changes in the mixed
925 and barrier layers in the western Equatorial Atlantic. *Braz. J. Oceanogr.* 53, 83–98.

926 Smith, J.E., Smith, C.M., Vroom, P.S., Beach, K.L., Miller, S., 2004. Nutrient and growth
927 dynamics of *Halimeda* tuna on Conch Reef, Florida Keys: Possible influence of internal
928 tides on nutrient status and physiology. *Limnol. Oceanogr.* 49, 1923–1936.
929 <https://doi.org/10.4319/lo.2004.49.6.1923>

930 Smith, K.A., Rocheleau, G., Merrifield, M.A., Jaramillo, S., Pawlak, G., 2016. Temperature
931 variability caused by internal tides in the coral reef ecosystem of Hanauma bay, Hawai‘i.
932 *Cont. Shelf Res.* 116, 1–12. <https://doi.org/10.1016/j.csr.2016.01.004>

933 Speer, K.G., Isemer, H.-J., Biastoch, A., 1995. Water mass formation from revised COADS
934 data. *J. Phys. Oceanogr.* 25, 2444–2457.

935 Sprintall, J., Gordon, A.L., Koch-Larrouy, A., Lee, T., Potemra, J.T., Pujiana, K., Wijffels, S.E.,
936 2014. The Indonesian seas and their role in the coupled ocean–climate system. *Nat.
937 Geosci.* 7, 487–492. <https://doi.org/10.1038/ngeo2188>

938 Sprintall, J., Gordon, A.L., Wijffels, S.E., Feng, M., Hu, S., Koch-Larrouy, A., Phillips, H.,
939 Nugroho, D., Napitu, A., Pujiana, K., Susanto, R.D., Sloyan, B., Peña-Molino, B., Yuan,
940 D., Riama, N.F., Siswanto, S., Kuswardani, A., Arifin, Z., Wahyudi, A.J., Zhou, H.,
941 Nagai, T., Ansong, J.K., Bourdalle-Badié, R., Chanut, J., Lyard, F., Arbic, B.K.,
942 Ramdhani, A., Setiawan, A., 2019. Detecting Change in the Indonesian Seas. *Front.
943 Mar. Sci.* 6.

944 Swift, J.H., Aagaard, K., 1981. Seasonal transitions and water mass formation in the Iceland
945 and Greenland seas. *Deep Sea Res. Part Oceanogr. Res. Pap.* 28, 1107–1129.
946 [https://doi.org/10.1016/0198-0149\(81\)90050-9](https://doi.org/10.1016/0198-0149(81)90050-9)

- 947 Tchilibou, M., Gourdeau, L., Lyard, F., Morrow, R., Koch Larrouy, A., Allain, D., Djath, B.,
948 2020. Internal tides in the Solomon Sea in contrasted ENSO conditions. *Ocean Sci.* 16,
949 615–635. <https://doi.org/10.5194/os-16-615-2020>
- 950 Tchilibou, M., Gourdeau, L., Morrow, R., Serazin, G., Djath, B., Lyard, F., 2018. Spectral
951 signatures of the tropical Pacific dynamics from model and altimetry: a focus on the
952 meso-/submesoscale range. *Ocean Sci.* 14, 1283–1301. <https://doi.org/10.5194/os-14-1283-2018>
- 954 Tchilibou, M., Koch-Larrouy, A., Barbot, S., Lyard, F., Morel, Y., Jouanno, J., Morrow, R.,
955 2022. Internal tides off the Amazon shelf during two contrasted seasons: interactions
956 with background circulation and SSH imprints. *Ocean Sci.* 18, 1591–1618.
957 <https://doi.org/10.5194/os-18-1591-2022>
- 958 Varona, H.L., Veleda, D., Silva, M., Cintra, M., Araujo, M., 2019. Amazon River plume
959 influence on Western Tropical Atlantic dynamic variability. *Dyn. Atmospheres Oceans*
960 85, 1–15. <https://doi.org/10.1016/j.dynatmoce.2018.10.002>
- 961 Vlasenko, V., Stashchuk, N., 2006. Amplification and Suppression of Internal Waves by Tides
962 over Variable Bottom Topography. *J. Phys. Oceanogr.* 36, 1959–1973.
963 <https://doi.org/10.1175/JPO2958.1>
- 964 Wang, X., Peng, S., Liu, Z., Huang, R.X., Qian, Y.-K., Li, Y., 2016. Tidal Mixing in the South
965 China Sea: An Estimate Based on the Internal Tide Energetics. *J. Phys. Oceanogr.* 46,
966 107–124. <https://doi.org/10.1175/JPO-D-15-0082.1>
- 967 Wentz, F.J., 2015. A 17-Yr Climate Record of Environmental Parameters Derived from the
968 Tropical Rainfall Measuring Mission (TRMM) Microwave Imager. *J. Clim.* 28, 6882–
969 6902. <https://doi.org/10.1175/JCLI-D-15-0155.1>
- 970 Whalen, C.B., Talley, L.D., MacKinnon, J.A., 2012. Spatial and temporal variability of global
971 ocean mixing inferred from Argo profiles. *Geophys. Res. Lett.* 39.
972 <https://doi.org/10.1029/2012GL053196>
- 973 Xie, S.-P., Carton, J.A., 2004. Tropical Atlantic variability: Patterns, mechanisms, and impacts.
974 Wash. DC Am. Geophys. Union Geophys. Monogr. Ser. 147, 121–142.
975 <https://doi.org/10.1029/147GM07>
- 976 Xu, P., Yang, W., Zhu, B., Wei, H., Zhao, L., Nie, H., 2020. Turbulent mixing and vertical
977 nitrate flux induced by the semidiurnal internal tides in the southern Yellow Sea. *Cont.*
978 *Shelf Res.* 208, 104240. <https://doi.org/10.1016/j.csr.2020.104240>
- 979 Yadidya, B., Rao, A.D., 2022. Projected climate variability of internal waves in the Andaman
980 Sea. *Commun. Earth Environ.* 3, 1–12. <https://doi.org/10.1038/s43247-022-00574-8>
- 981 Zalesak, S.T., 1979. Fully multidimensional flux-corrected transport algorithms for fluids. *J.*
982 *Comput. Phys.* 31, 335–362. [https://doi.org/10.1016/0021-9991\(79\)90051-2](https://doi.org/10.1016/0021-9991(79)90051-2)
- 983 Zaron, E.D., 2019. Baroclinic Tidal Sea Level from Exact-Repeat Mission Altimetry. *J. Phys.*
984 *Oceanogr.* 49, 193–210. <https://doi.org/10.1175/JPO-D-18-0127.1>

986

987

988

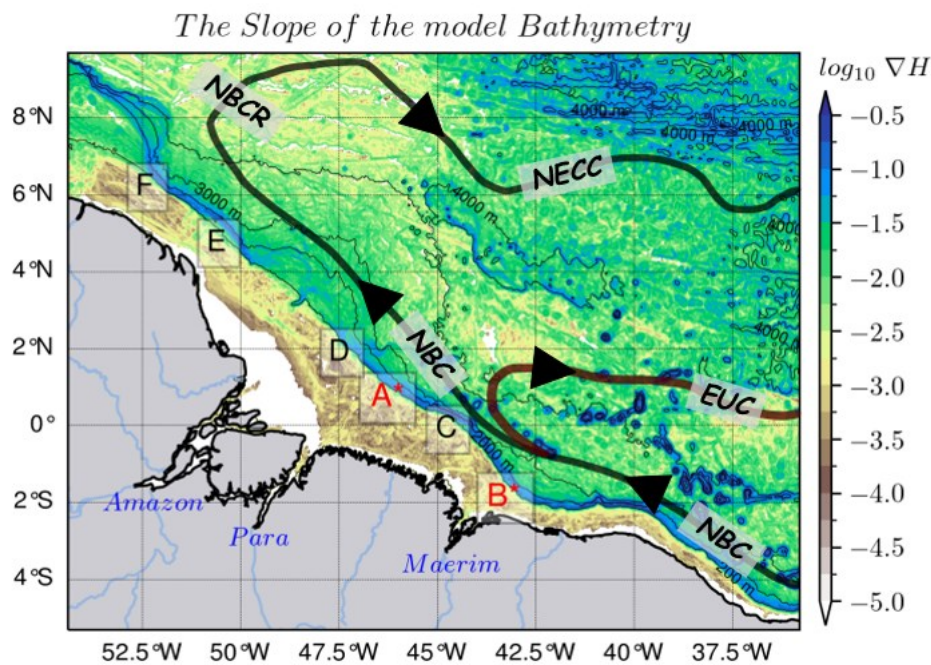
989

990

991

992

993
994
995
996
997
998
999
1000



1001
1002
1003
1004
1005
1006
1007
1008
1009
1010
1011
1012
1013

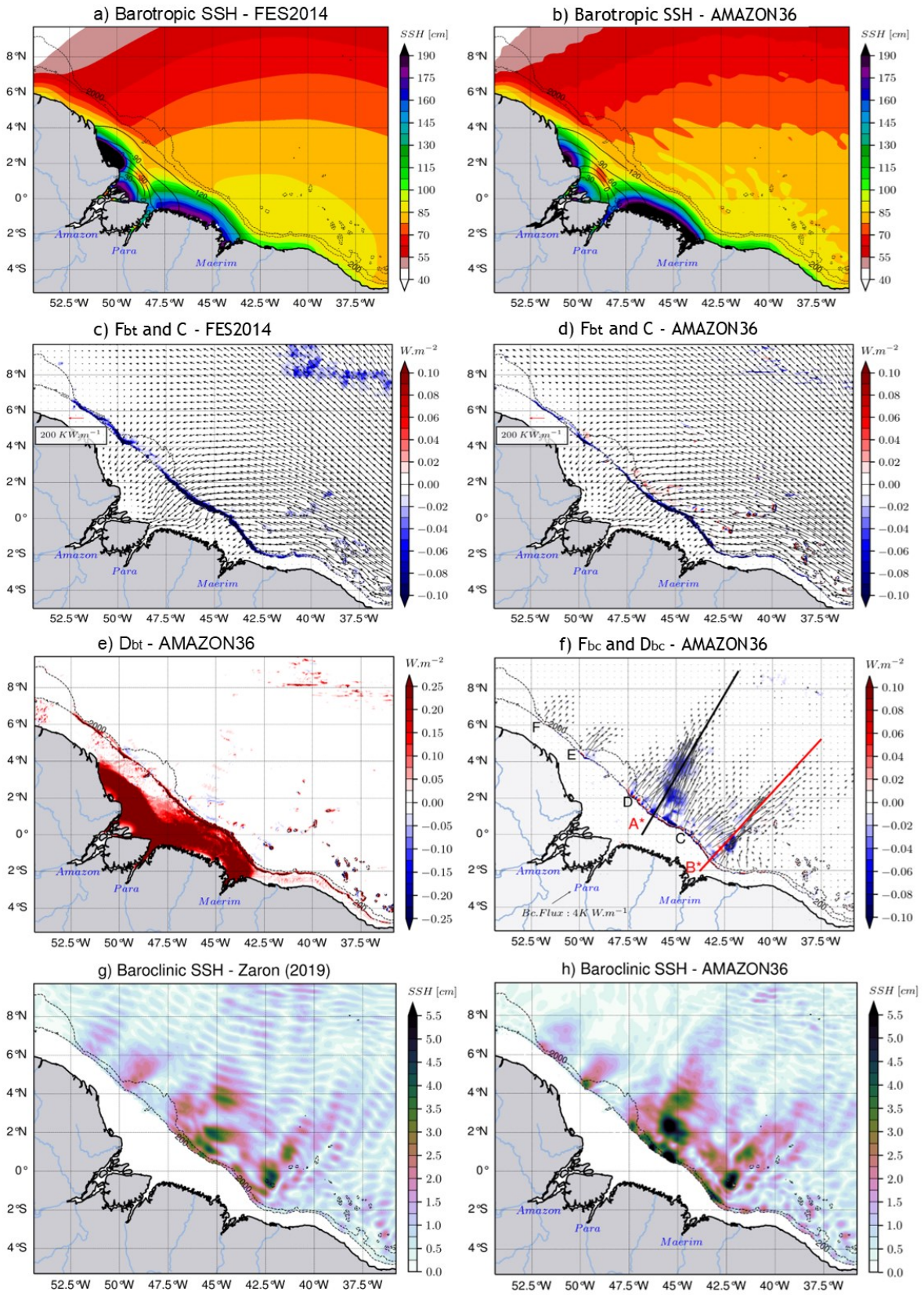
Figure 1. The horizontal gradient (∇H) of the model's bathymetry with different internal tides generation sites (A, B*, C, D, E and F) along the high slope (blue color shading) of the shelf break, with the two main sites A* and B* (in red), as reported in Magalhaes et al. (2016) and Tchilibou et al. (2022). Solid bold lines represent a schematic view of the circulation (as described by Didden and Schott, 1993; Richardson et al., 1994; Johns et al., 1998; Bourles et al., 1999a; Schott et al., 2003; Garzoli et al., 2004) with NBC, NBCR and NECC tracks in black, and the EUC track in brown red. Tin black contours are 200 m, 2000 m, 3000 m and 4000 m isobaths.*

1014

1015

1016

1017



bt : barotropic ; bc : baroclinic
 F : energy flux ; C : barotropic-to-baroclinic energy conversion ; D : dissipation

1018

1019 *Figure 2. Coherent (or stationary) characteristics of the M_2 tides. Barotropic sea surface height*

1020 *(color shading) and its phase (solid contours) for (a) FES2014 and (b) the model, barotropic*
1021 *energy flux (black arrows) with the energy conversion rate (color shading) for (c) FES2014*
1022 *and (d) the model, (e) the model depth-integrated barotropic energy dissipation, (f) the model*
1023 *depth-integrated baroclinic energy flux (black arrows) and the depth-integrated baroclinic*
1024 *energy dissipation (color shading) with transect lines along IT trajectories A* (black) and B**
1025 *(red), the baroclinic sea surface height from (g) Zaron (2019) and (h) the model. Data from the*
1026 *model are the mean value over the year 2015. For all panels, dashed black lines represent the*
1027 *200 m and 2000 m isobaths of the model bathymetry.*

1028

1029

1030

1031

1032

1033

1034

1035

1036

1037

1038

1039

1040

1041

1042

1043

1044

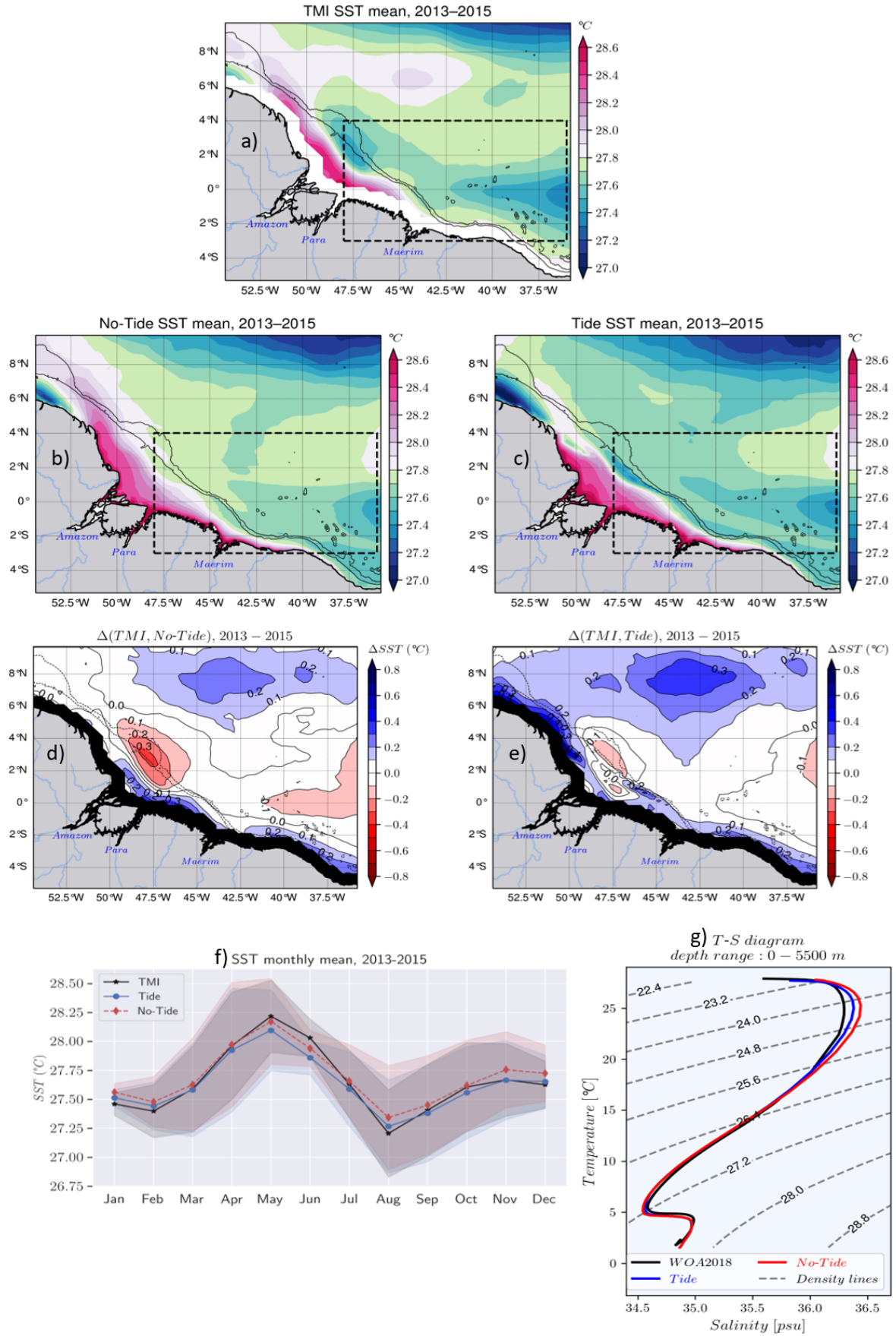
1045

1046

1047

1048

1049



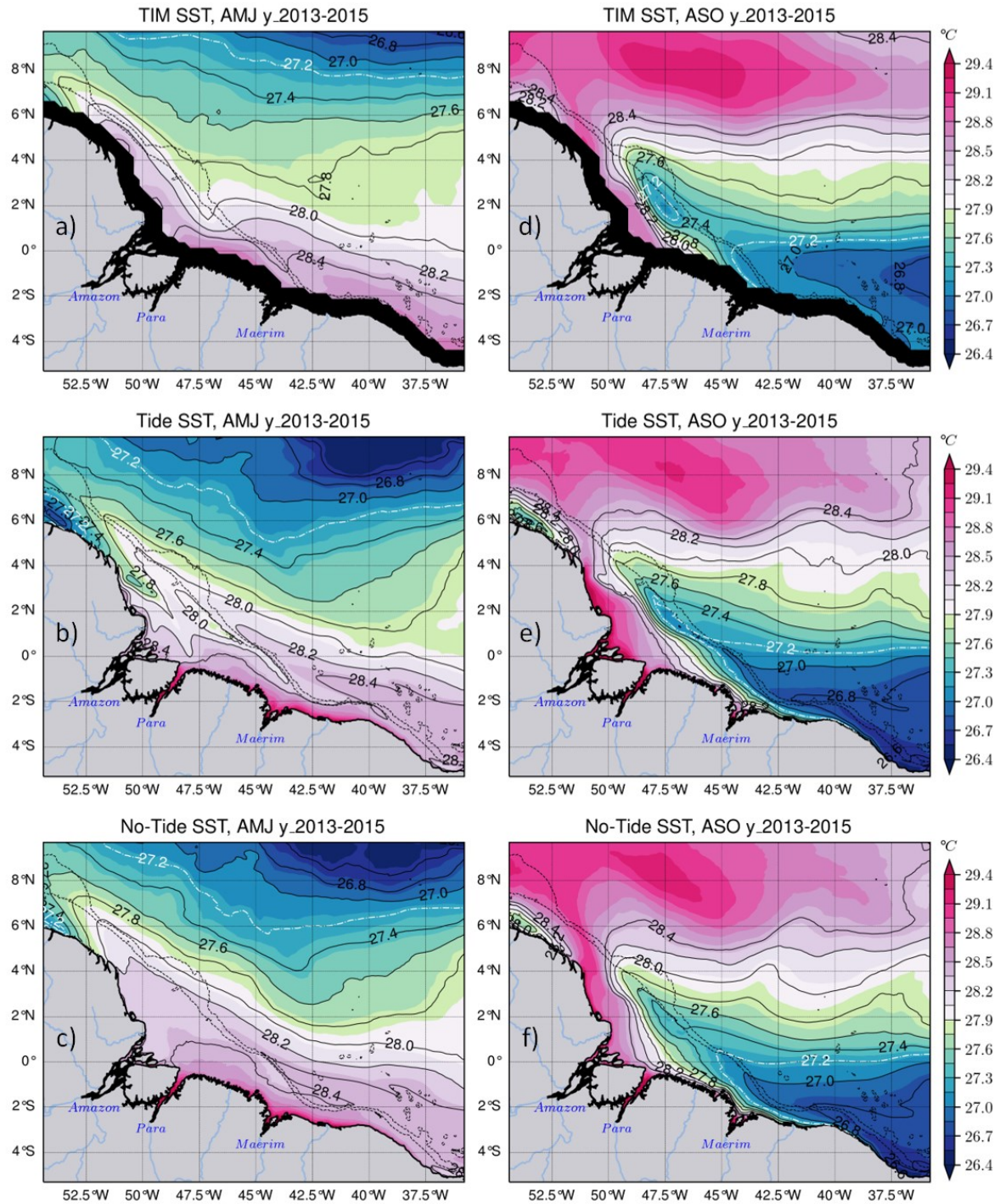
1051 *Figure 3. Validation of the model temperature for the whole period 2013-2015. Mean SST for*
1052 *(a) TMI with its black coastal mask, (b) the tidal simulation, (c) the non-tidal simulation, the*
1053 *difference (bias) in SST between TMI and (d) the tidal simulation and (e) the non-tidal*
1054 *simulation, (f) the seasonal cycle of the SST of the three products averaged within the dashed*
1055 *line box in upper panels covering IT pathways with values masked below the 200 m isobath,*
1056 *bands indicate variability according to standard deviation. Solid black lines in panels a-c and*
1057 *dashed black lines in panels d-e represent the 200 m and 2000 m isobaths from the model*
1058 *bathymetry, while solid black lines in panels d-e represent bias contours. (g) Temperature-*
1059 *Salinity (T-S) diagram of the mean properties in the same area as (f) from observed WOA2018*
1060 *climatology (black line), the tidal simulation (blue line) and non-tidal simulation (red line) for*
1061 *the water column from surface to 5500 m depth, dashed gray lines represent density (σ_θ)*
1062 *contours.*

1063

1064

1065

1066



1067

1068

1069

1070

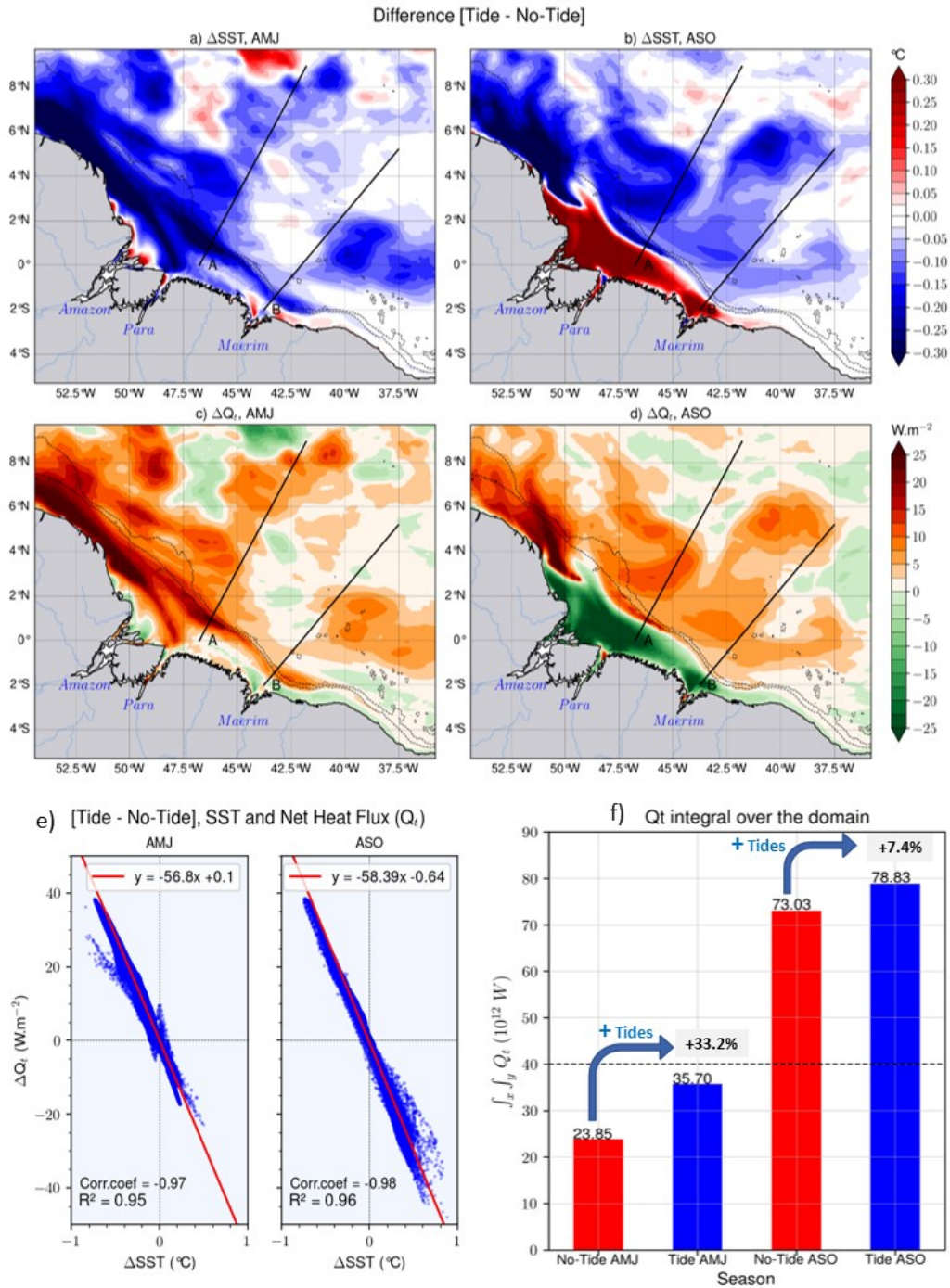
1071

1072

1073

1074

Figure 4. 2013-2015 seasonal SST mean. The left panels stand for the AMJ season for TMI with its black coastal mask, the tidal simulation and the non-tidal simulation, respectively for the upper-left, center-left and lower-left panel; the same in the panels on the right but for the ASO season. The dashed white and black solid lines represent the temperature contours. Dashed black lines in all panels stand for the 200 m and 2000 m isobaths from the model bathymetry.



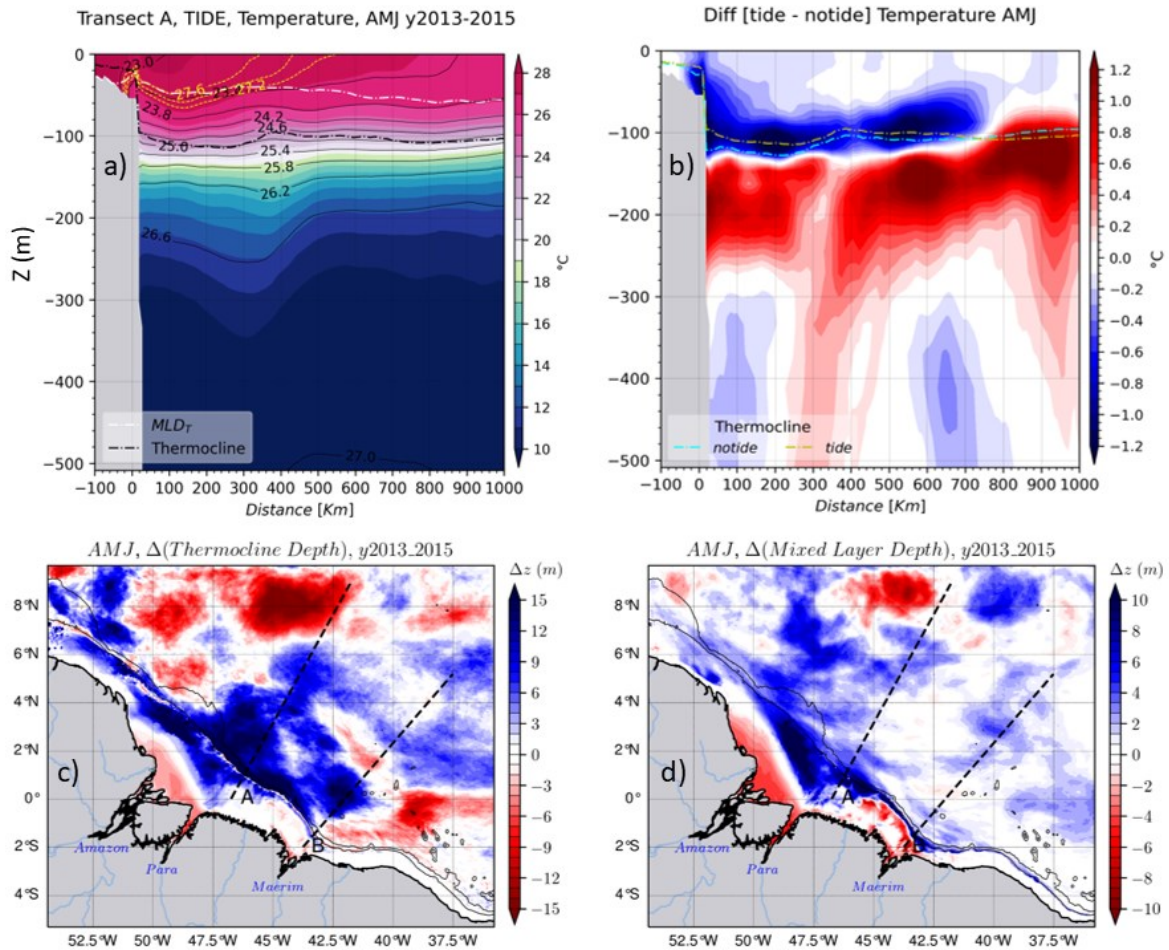
1075

1076 *Figure 5. Relationship between the SST and the atmosphere-to-ocean net heat flux (Q_t): SST*
 1077 *anomaly [Tide - No-Tide] in AMJ (a) and ASO (b) seasons, Q_t anomaly in AMJ (c) and ASO*
 1078 *(d) seasons, (e) correlation between Q_t anomaly and SST anomaly for each season, (f) domain*
 1079 *integrated Q_t for both seasons of each simulation.*

1080

1081

1082



1083

1084 *Figure 6. Some water mass properties for the AMJ season: (a) vertical section of the*
 1085 *temperature of the tidal simulation following the transect A, the yellow dashed and the solid*
 1086 *black lines are the temperature and density (σ_θ) contours respectively, the black and white*
 1087 *ticker dashed lines are the thermocline and MLD respectively, (b) the temperature anomaly for*
 1088 *the same vertical section, yellow and cyan dashed lines are the thermocline depth for the tidal*
 1089 *and non-tidal simulations respectively, (c) thermocline depth anomaly and (d) MLD anomaly*
 1090 *for the whole domain. When the MLD or the Thermocline depth anomaly are colored in blue*
 1091 *(vs red) it means that the tides rise (vs deepen) them. Solid black lines in lower panels stand*
 1092 *for the 200 m and 2000 m isobaths from the model bathymetry.*

1093

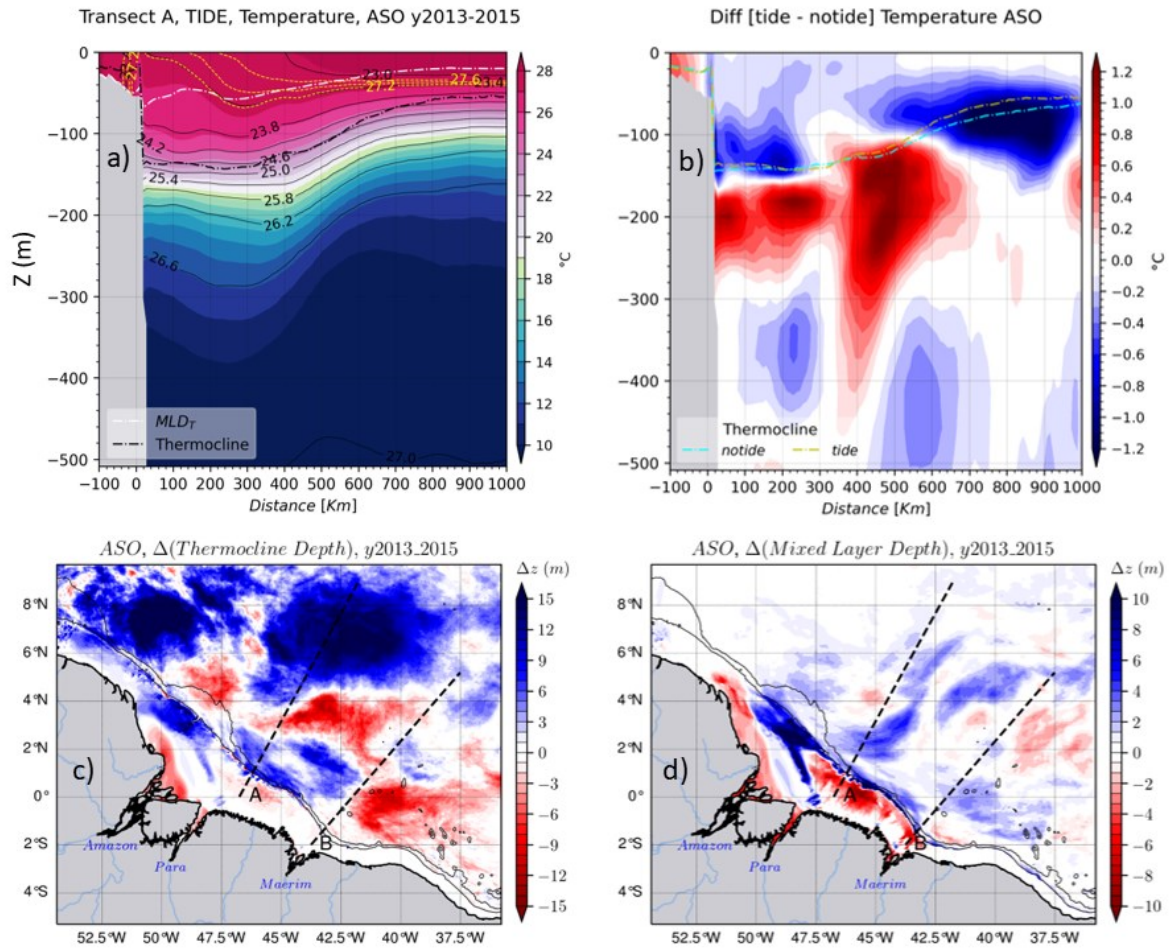
1094

1095

1096

1097

1098



1099

1100 *Figure 7. Same as figure 6 but for the ASO season.*

1101

1102

1103

1104

1105

1106

1107

1108

1109

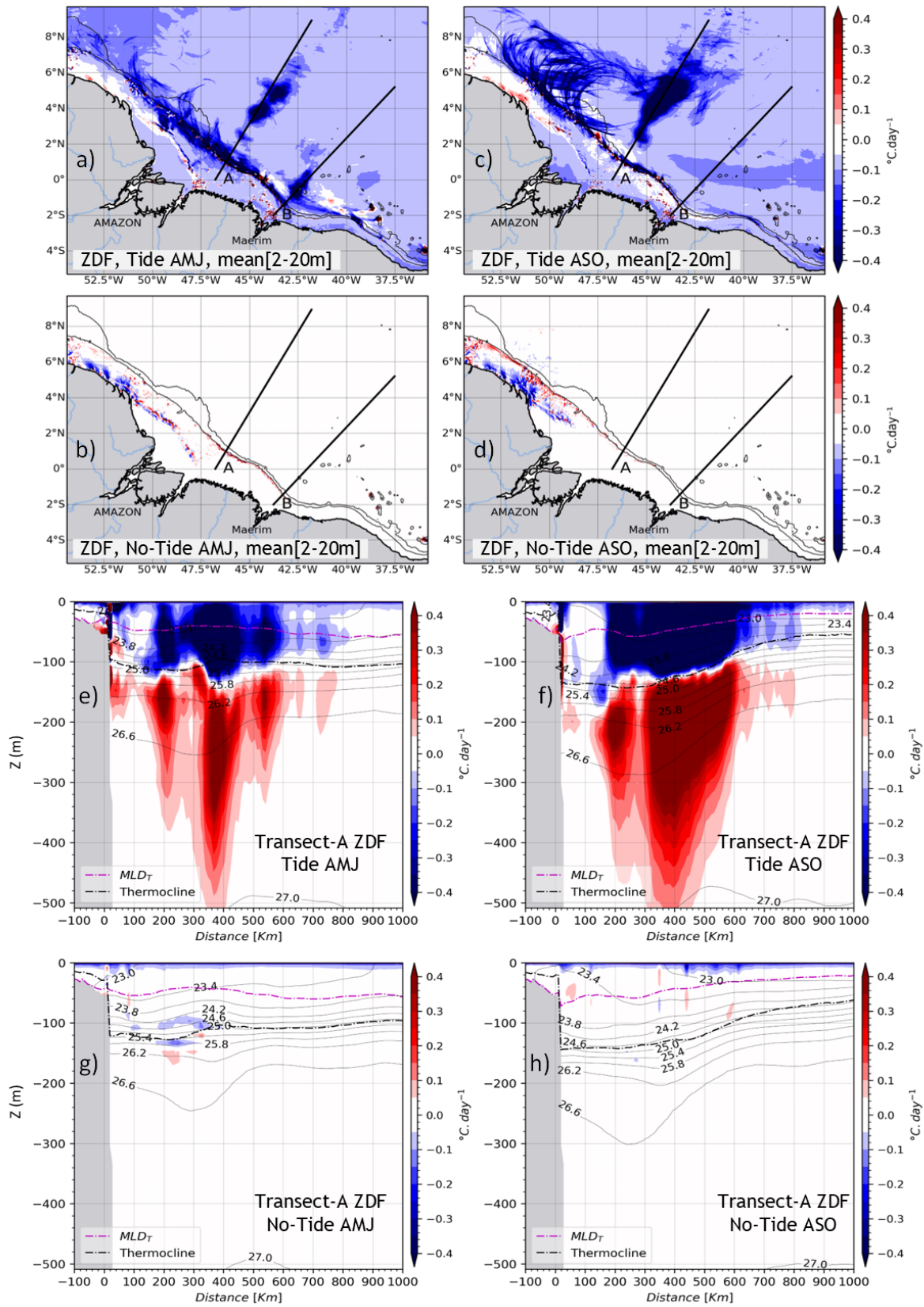
1110

1111

1112

1113

1114



1115

1116

1117

Figure 8. The vertical diffusion tendency of temperature (ZDF) for both seasons. The vertical mean between 2–20 m for AMJ season in tidal (a) and non-tidal (b) simulation; then for ASO

1118 *season in tidal (c) and non-tidal (d) simulations. Vertical sections of ZDF following the transect*
1119 *A for AMJ season in the tidal (e), for ASO season in non-tidal (f) simulations; then for AMJ*
1120 *season in the non-tidal (g) and for ASO season in the non-tidal (h) simulations. The black and*
1121 *magenta dashed lines are the thermocline depth and MLD respectively. Solid black lines in*
1122 *panels a-d stand for the 200 m and 2000 m isobaths from the model bathymetry, while in panels*
1123 *e-h, they represent the density (σ_θ) contours.*
1124

1125

1126

1127

1128

1129

1130

1131

1132

1133

1134

1135

1136

1137

1138

1139

1140

1141

1142

1143

1144

1145

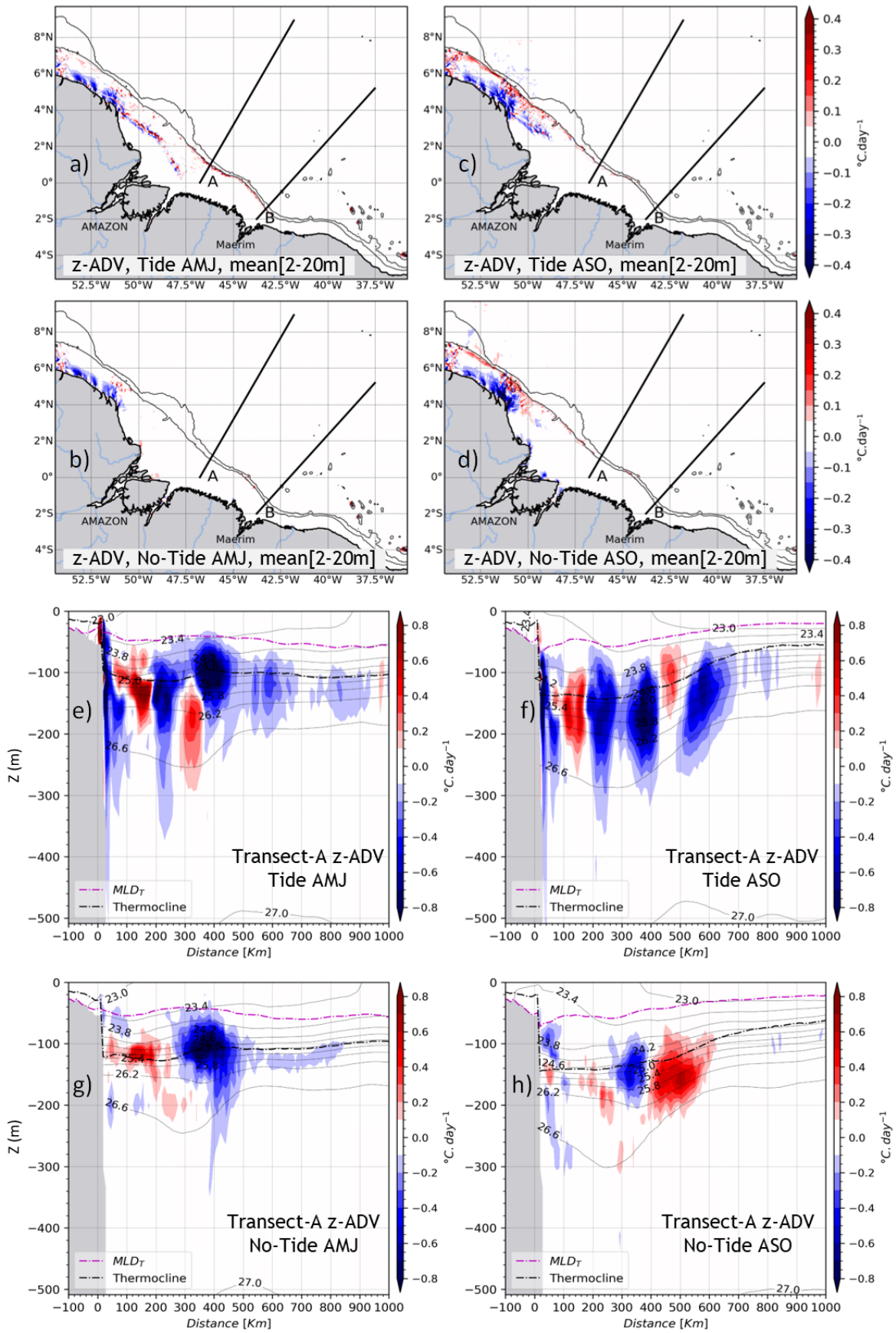
1146

1147

1148

1149

1150



1152 *Figure 9. Same as figure 8, but for the vertical advection tendency of temperature (z -ADV).*

1153

1154

1155

1156

1157

1158

1159

1160

1161

1162

1163

1164

1165

1166

1167

1168

1169

1170

1171

1172

1173

1174

1175

1176

1177

1178

1179

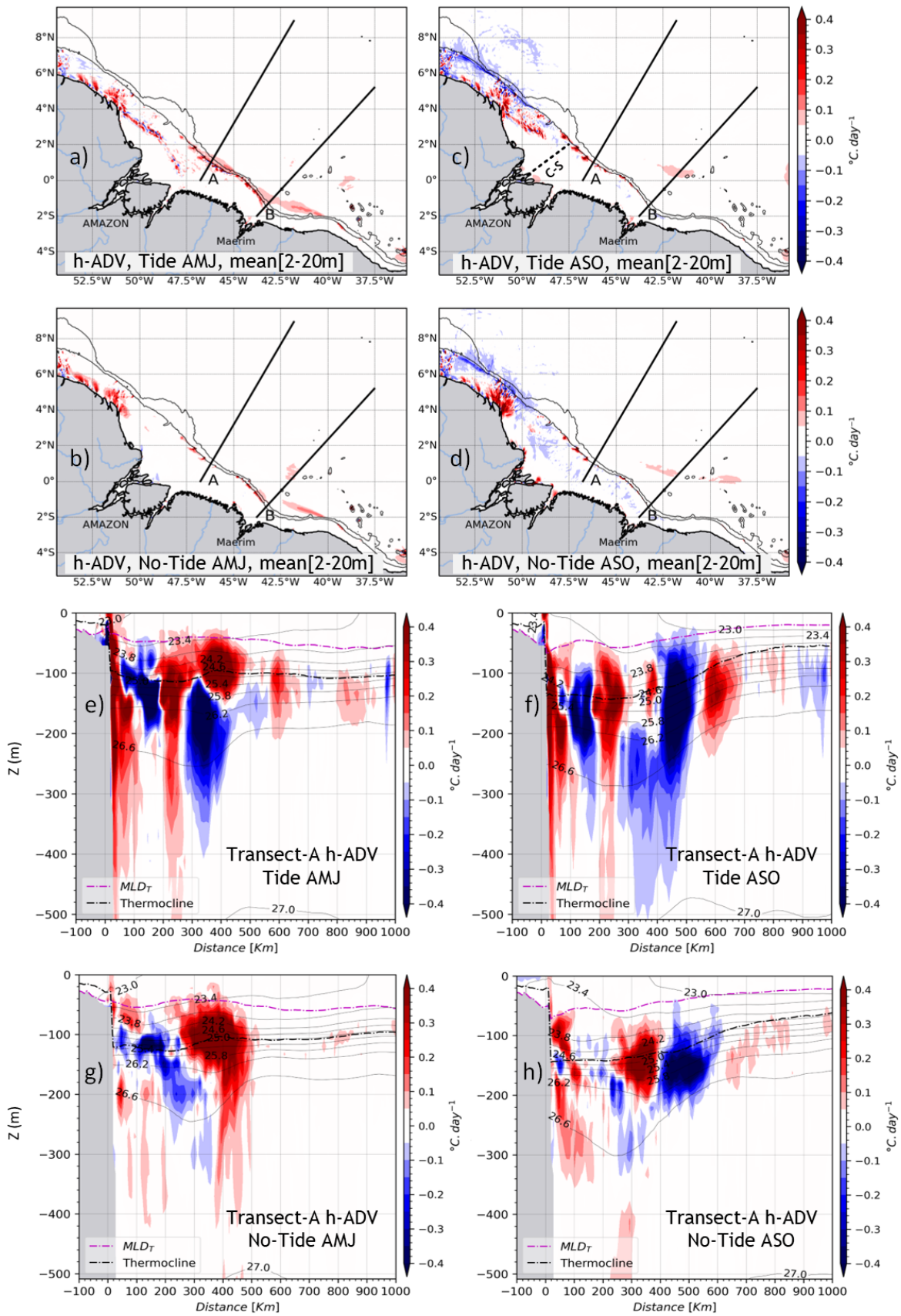
1180

1181

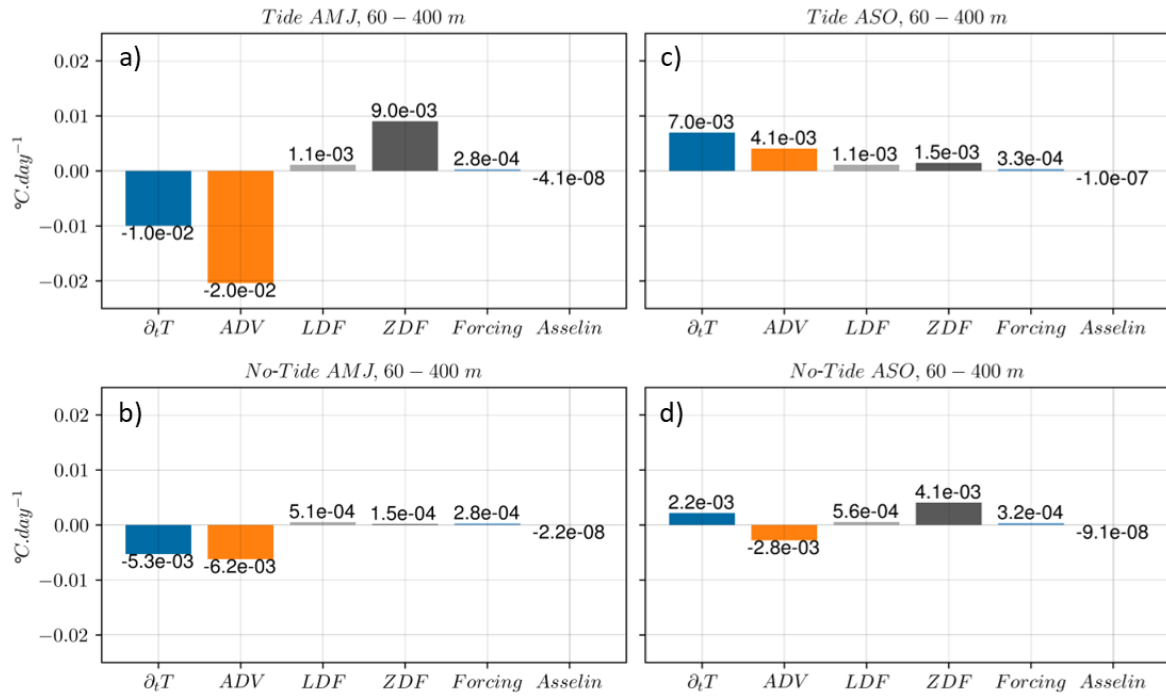
1182

1183

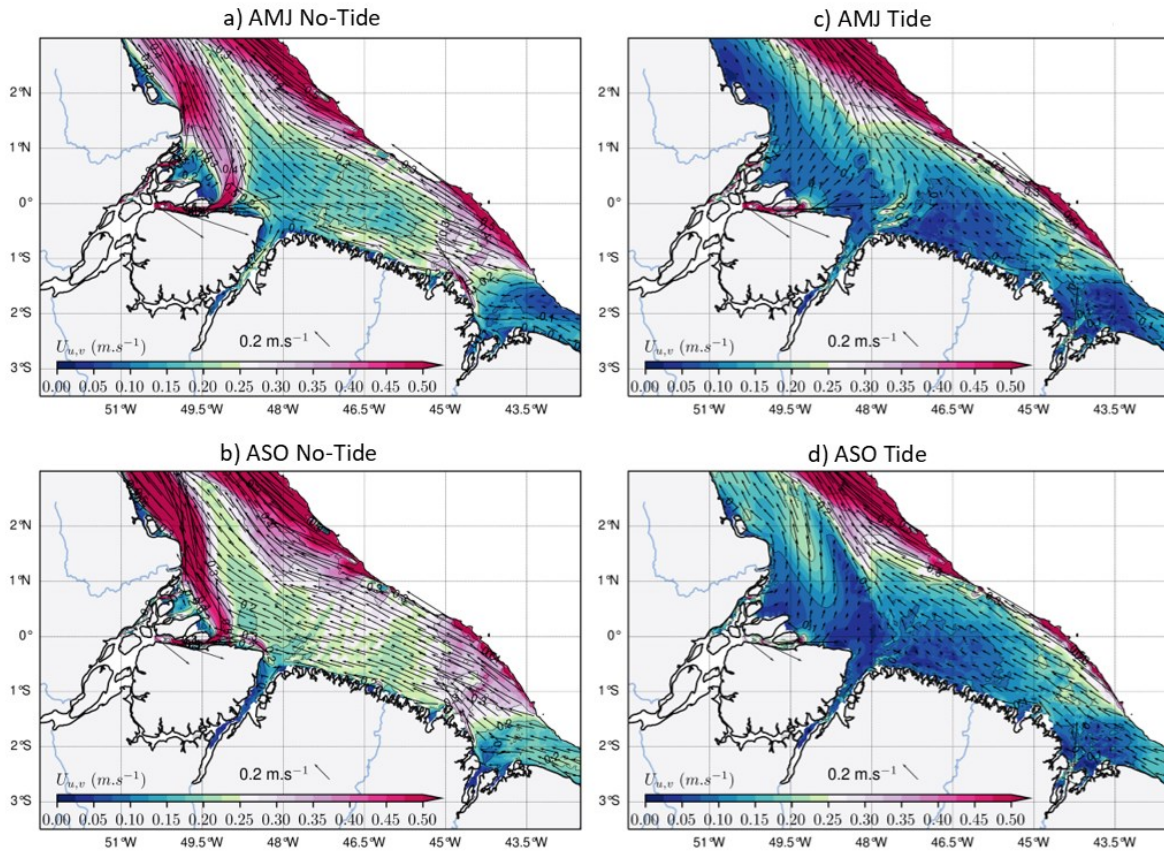
1184



1186 Figure 10. Same as figure 8 but for the horizontal advection of temperature ($h\text{-}ADV = x\text{-}ADV$
 1187 $+ y\text{-}ADV$). The dashed line from the Amazon River mouth toward the outer shelf in the panel
 1188 (b) indicates the cross-shore transect (C-S) used further on.
 1189



1190 Figure 11. Trends balance averaged in region around IT trajectories between 48°W–40°W and
 1191 0°N–6°N, and below the MLD between 60-400 m depth. Upper panels are for the tidal
 1192 simulation and lower panels for the non-tidal simulation, while left and right panels are for the
 1193 AMJ and ASO seasons respectively. ZDF is the dominant term of the heat budget equation (see
 1194 section II.3.2) within the mixed-layer to explain temperature changes in upper layers.
 1195



1196

1197 *Figure 12. The seasonal mean of the current ($U_{u,v}$) at the shelf averaged between the surface*
 1198 *and 50 m: the non-tidal simulation in the left panels and the tidal simulation in the right panels.*
 1199 *The upper panels stand for the AMJ season, while the lower stand for the ASO season. The*
 1200 *color shading is the modulus of the current and the black arrows represent its direction. Values*
 1201 *beyond the 200 m isobath are masked.*

1202

1203

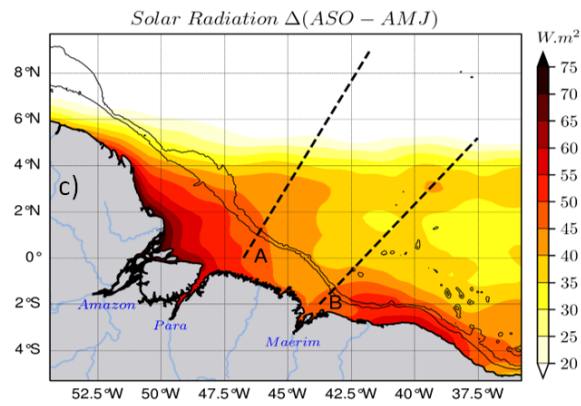
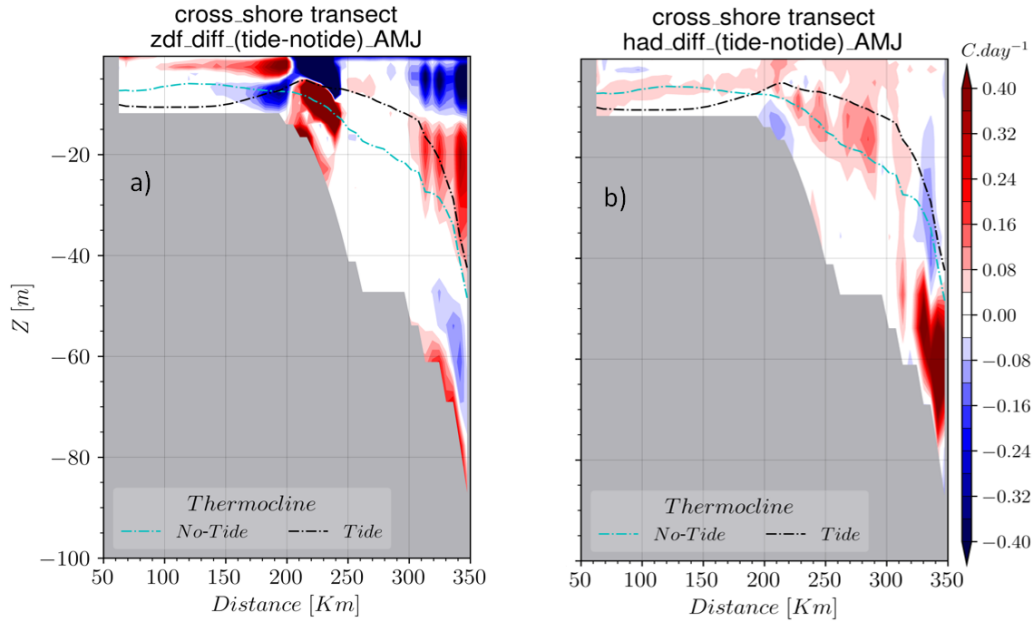
1204

1205

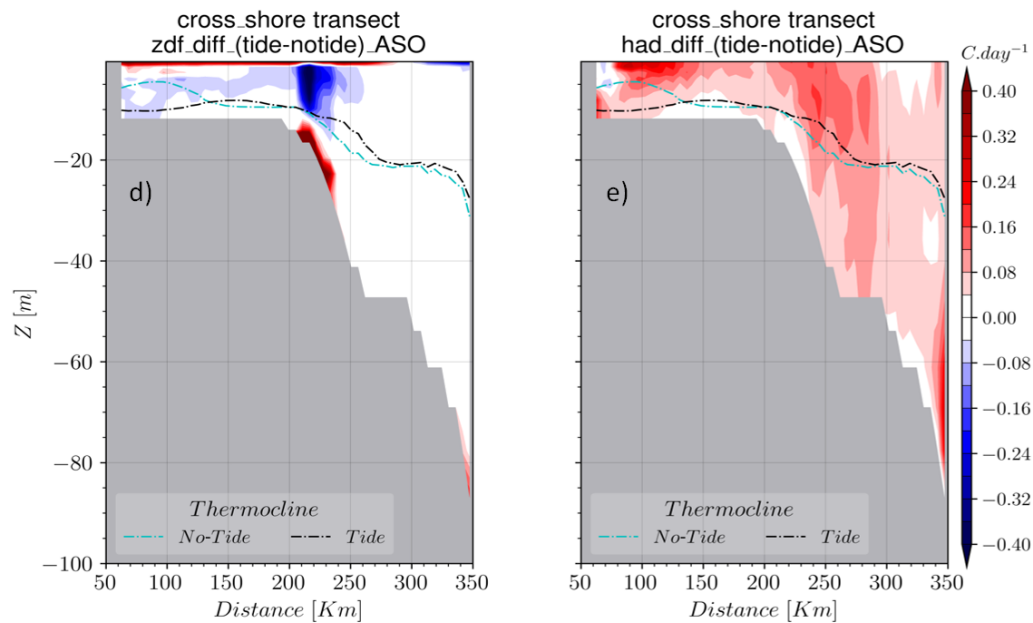
1206

1207

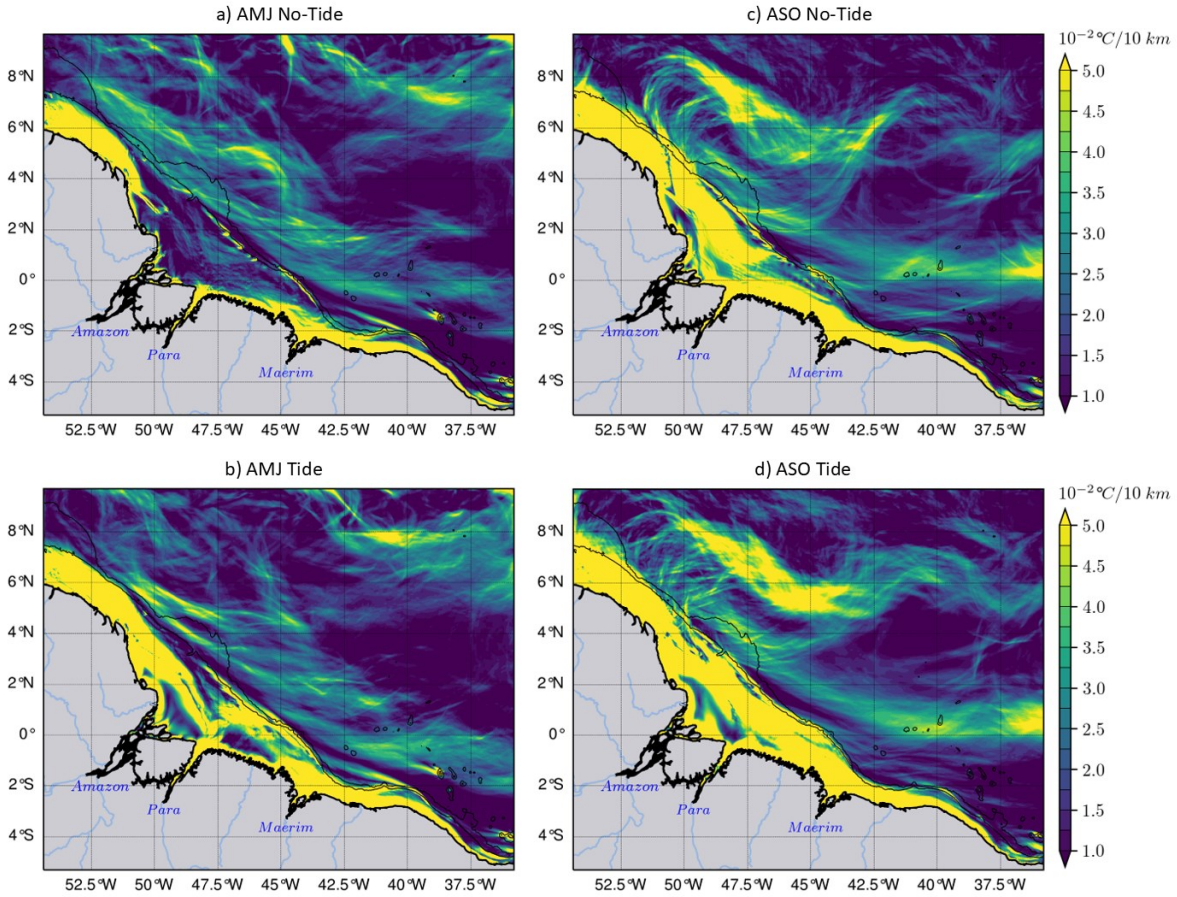
1208



Solar radiation (Q_s) increases in the ASO season:
 > 30 $W \cdot m^2$ offshore
 > 60 $W \cdot m^2$ over the shelf



1210 *Figure 13. The cross-shore transect of ZDF anomaly for (a) AMJ and (b) ASO seasons, then*
 1211 *for h-ADV anomaly for (d) AMJ and (e) ASO seasons ; (c) Difference in solar radiation*
 1212 *between ASO and AMJ seasons. Solar radiation increases during the ASO season, with greater*
 1213 *intensity on the shelf.*
 1214



1215
 1216 *Figure 14. The horizontal gradient of the Temperature (∇T) averaged between 2–20 m : the*
 1217 *AMJ season in the left panels and ASO season in the right panels, the simulations without the*
 1218 *tides in the upper panels, and with tides in the lower panels. During the ASO season, the NBC*
 1219 *retroreflects and eddy activity intensifies in the north-west. Therefore, ∇T emphasizes eddy-like*
 1220 *fronts at the same location as eddy-like patterns in ZDF (see Fig.9b).*
 1221

1222
 1223
 1224
 1225
 1226